A Minimally-Invasive Robotic Spinal Surgical System for Anterior Lumbar Nerve Decompression

Qingxiang Zhao[1†], Xiandi Wang[2†], Xin Zhong[1], Runfeng Zhu[1], Peizhi Zhou[3], Dan Pu[2], Baitao Lin[1], Tao Li[1], Shiyuan Sui[1], Haonan Zhou[1], Yuxi Cheng[1], Hao Zheng[4], Henry K. Chu[4], Jiancheng Zeng[5*], Kang Li[1,6*]

[1]West China Biomedical Big Data Center, West China Hospital, Sichuan University, Chengdu &610041, China.

[2] Medical Simulation Center, West China Hospital, Sichuan University, Chengdu &610041, China.

[3] Department of Neurosurgery, West China Hospital, Sichuan University, Chengdu &610041, China.

[4] Department of Mechanical Engineering, The Hong Kong Polytechnic University, Kowloon, Hong Kong SAR.

[5] Department of Orthopedics, West China Hospital, Sichuan University, Chengdu &610041, China.

[6] Sichuan University - Pittsburgh Institute, Sichuan University, Chengdu &610041, China.

[*]Corresponding author. Email: likang@wchscu.cn and tomzeng5@163.com

[†]These authors contributed equally to this work.

Lumbar degenerative diseases, primarily caused by pathological tissues compressing spinal nerves, typically necessitate surgical intervention—specifically lumbar nerve decompression—to alleviate pain. Although the anterior decompression approach demonstrates notable advantages such as reduced bleeding and shorter postoperative hospitalization stay compared to the conventional posterior approach, patients may still experience incomplete decompression due to various instrumental shortcomings, including restricted visibility and insufficiency of distal dexterity. In this study, we present a robotic surgical system for minimally invasive anterior lumbar nerve decompression, which comprises three slender

robotic arms (2 mm in outer diameter) with high dexterity (18 degrees of freedom), facilitating effective navigation through narrow intervertebral disc space to reach the posterior area. Each robot arm is based on concentric push-pull robot (CPPR) structure, forming three robotized instruments: an endoscope for visualization, a laser optical fiber for hemostasis and resection, and a gripper for tissue manipulation. These components are integrated through the hollow lumen of a slender trocar, and multi-instrument coordination enables effective decompression procedure with wide view. System performance was first validated using a 3D-printed vertebral phantom model to confirm accessibility to bilateral articular processes. Subsequently, in vivo animal experiment and human cadaver tests were conducted to further demonstrate the full capabilities in performing minimally invasive lumbar nerve decompression. This study demonstrates the potential of the robotic system to facilitate surgical procedures in narrow, confined, and tortuous anatomical spaces, addressing the key limitations of conventional instruments in anterior lumbar nerve decompression.

MicroSpine, a robotic system designed for minimally invasive anterior lumbar nerve decompression.

Introduction

Lumbar degenerative diseases (*1*), primarily caused by aging and sedentary lifestyles, impose substantial lower back and leg pain on affected patients. Notably, these conditions are no longer confined to the geriatric population but are increasingly prevalent among young adults. Studies have reported approximately 266 million annual cases of lower back pain attributed to degenerative spine diseases (*2*), with projections suggesting that around 890 million individuals will be affected globally by 2050 (*3*). The core pathogenic mechanism involves the compression of spinal canal nerves by degenerative structures (Figure S1 (A)), including disc herniation, osteophyte formation, and ligamentum flavum hypertrophy (Figure S1 (B)) (*4*). Consequently, surgical decompression (resection of these degenerative structures) and spinal fusion (placement of an interbody fusion cage (Figure S1 (C))) have become important clinical procedures to alleviate symptoms and restore spinal stability (*5–8*). Nevertheless, current surgical approaches either necessitate extensive incisions or

result in incomplete decompression due to the inherent limitations of available instruments. To address these challenges, we have developed a robotic system that leverages the minimally invasive and low-hemorrhage benefits of the anterior approach. By utilizing slender, highly dexterous robotic arms equipped with integrated surgical tools, our objective is to facilitate direct, precise, and complete lumbar nerve decompression through a minimally invasive corridor.

Posterior and anterior surgical techniques both achieve decompression and fusion, but they have weaknesses. The traditional posterior approach is widely employed to directly resect degenerative spinal tissues located in the posterior spinal area (*9*). In this procedure, the patient's body is in a prone position, and the surgeon makes an incision to dissect the skin and paraspinal muscles for adequate vertebral exposure (Figure S1 (D)). Direct decompression is achieved by resecting the pathological posterior laminae and articular processes, thereby relieving lumbar nerve compression. Although the posterior decompression approach achieves over 85% symptomatic relief (*10*), it is concurrently associated with intraoperative blood loss of 300 to 500 mL (*11*) and a 21.6% risk of complications (*12, 13*). In contrast, the anterior approach (*14*) utilizes a small lumbar incision to access the target vertebra through a retroperitoneal anatomical corridor (Figure S1 (E)), followed by interbody fusion cage implantation. Oblique Lateral Interbody Fusion (OLIF) (*15*) is a prominent anterior technique characterized by minimal muscle damage and reduced intraoperative blood loss, which is typically around 30 mL (*16*). Despite these advantages, clinical evidence shows that OLIF provides only moderate efficacy (65%–78%) for central canal stenosis and remains ineffective against posterior pathologies, such as facet joint hypertrophy (*17*). This limitation results in a 32.4% postoperative residual symptom rate, primarily due to unaddressed posterior compression (*18*). As illustrated in Figure S1 (F), the inherently rigid and straight configuration of conventional surgical instruments severely constrains the operational workspace and visual field necessary for the precise resection of degenerative structures. Consequently, surgeons rely on interbody fusion cage implantation to expand space for the compressed nerves and treat spondylolisthesis. However, this indirect technique fails to physically resect posterior degenerative tissues, such as the superior articular processes, thereby resulting in incomplete decompression. In modern spinal surgery, conventional instruments remain rigid, straight, and often oversized for accessing the constricted posterior region (*19*), which underscores the urgent clinical necessity for advanced instrumentation to enhance OLIF decompression outcome.

Minimal invasiveness is an important unmet need in modern surgery, where the inherent benefits of anterior decompression have catalyzed the development of advanced instrumentation to enhance visualization and maneuverability within confined operative spaces. In spine surgery, angled endoscopes (*20, 21*), microscopes (*22*), and headlight-loupe combinations (*23*) have been clinically used to augment visual clarity. However, achieving comprehensive visualization remains challenging despite high-resolution imaging, primarily due to limited distal dexterity for navigating tortuous anatomical routes (*24*) and visual occlusion resulting from venous plexus hemorrhage (*25*). An estimated 46.2%–58.7% of the posterior canal wall remains obscured in conventional practice (*26*). A miniaturized endoscopic camera integrated into a steerable robotic arm, analogous to the Da Vinci SP system (*27, 28*), represents a promising solution to these constraints, but the size is not suitable for this procedure. To effectively support OLIF, robotic instruments must fulfill three fundamental requirements: reachability, visibility, and maneuverability within the narrow spinal anatomy. First, slenderness is an absolute prerequisite, as the intervertebral disc space typically measures only 8 to 13 mm in height (*29*). This narrow corridor is the only path through which instruments can navigate to access the posterior area. Furthermore, because surgical resection generally necessitates the simultaneous deployment of multiple tools—such as a gripper for tissue manipulation and a rongeur for resection (*30*)—only miniaturized instruments can operate effectively within this confined anatomy. Second, distal dexterity is essential, as the superior and inferior articular processes are located at the posterior side of the spinal canal. This anatomical positioning makes it exceedingly difficult for conventional straight instruments to navigate the required tortuous routes. Finally, the steerable segments of the instruments must provide enough rigidity to effectively retract and strip elastic spinal tissues (*31*).

The structural design of these instruments is thus critical. Researchers have developed continuum robots for surgical applications, including tendon-driven articulated linkage robots (*28, 32*) (8 mm diameter, single-segment bending) and fluid-driven flexible manipulators (*33–35*), but these face stiffness and dexterity insufficiency. Furthermore, electroactive polymers (*36*) and magnetically driven robots (*37*) typically require bulky external systems for actuation. One promising architecture is the concentric tube robot (CTR), which features a hollow lumen and a slender robotic body (*38–40*). Nevertheless, CTRs are predominantly fabricated from nickel-titanium (Nitinol) alloys, which possess a Young's modulus of only approximately 40–75 GPa (*41*). In comparison, stainless

steel offers a higher Young's modulus of approximately 200 GPa. The lower modulus of Nitinol-based structures can result in undesirable rigidity (insufficient stiffness) when interacting with resistant spinal tissues. To address these limitations, we integrated the concentric push-pull robot (CPPR) architecture (*42, 43*) to develop a robotic platform which we call MicroSpine for minimally invasive lumbar nerve decompression (Figure S1 (G)). Inspired by the configuration of single-port, multi-arm surgical robots —similar to the triple-arm system proposed by Bruns et al. (*44*) for transnasal surgery —the MicroSpine system utilizes CPPR-based instruments featuring specialized tenon-mortise slits. This work leverages the unique advantages of these instruments, which are characterized by slenderness, a hollow lumen, relatively high structural stiffness, and notable bending curvature.

Compared with manual instrument manipulation by surgeons at the bedside, robot-assisted surgery provides distinct clinical benefits, including the simultaneous control of multiple instruments, effective tremor elimination, digitized and traceable procedural data, and reduced radiation exposure for the surgical team (*45–47*). Notable progress has been made in spinal robotic systems, including precision intraoperative navigation (Renaissance, Mazor Robotics (*48*)), real-time imaging (ExcelsiusGPS, Globus Medical (*49*)), and lumbar facet fixation systems (CAVUX FFS-LX, Providence Medical Technology (*50*)). The instruments on these systems are either straight or have limited distal steerability, making them inadequate for traversing the complex posterior spinal anatomy and performing complete decompression procedure via an oblique lumbar route.

In this work, we designed slender, highly dexterous CPPR-based instruments to navigate and manipulate within the confined and complex lumbar vertebral anatomy. To form the steerable and passive compliant segments, tenon-mortise slits and 'I'-shaped slits were manufactured on hollow steel tubes, respectively. Each robotic instrument features a 2 mm outer diameter (OD) and 0.9 mm inner diameter (ID), providing a hollow lumen for tip tool integration. With 6 degrees of freedom (DoF) and a dual-segment architecture, the instruments facilitate flexible resection of degenerative tissues while maintaining a comprehensive endoscopic field of view. Three slender instruments are integrated into a single 8 mm-OD trocar, supported by a compact actuation unit for high-precision control. We further developed an optimization-based inverse kinematics model for the redundant robotic instrument, achieving a 0.9 mm root-mean-square error (RMSE) in open-loop path-following tasks. To address the challenges of resecting hard osseous tissues with

miniaturized instruments, we integrated a thulium laser fiber to deliver energy to the confined spinal anatomy; this laser also serves to cauterize soft tissues, such as the venous plexus, for effective hemostasis with saline circulation. The MicroSpine system is designed to achieve direct, complete, and minimally invasive anterior lumbar nerve decompression via a single 3 cm incision. The system's performance was systematically validated, beginning with reachability assessments to bilateral articular processes using a 3D-printed, patient-specific vertebral phantom model, followed by in vivo animal experiments and human cadaver tests. Our findings indicate that this robot-assisted protocol enables efficient decompression, typically completed within 15 minutes with an estimated intraoperative blood loss of only 5 mL. Consequently, the MicroSpine system expands surgical indications for OLIF, including disc herniation, articular process hypertrophy, and ligament hypertrophy.

Results

Robotic System Design

The robotic system primarily consists of a bedside robot (Figure 1 (A)) and a surgeon control console (Figure 1 (B)). To minimize radiation exposure, the control console can be strategically positioned either adjacent to the operating table or in a separate room. A custom cart-mounted rigid robotic arm (xMateER7 RPO, ROKAE, Shenzhen, China) accurately positions the trocar at the patient's surgical site. Surgeons control the system via two joysticks, receiving real-time visual feedback from both a steerable endoscopic camera and a fixed trocar-mounted camera. Laser energy for resecting degenerative spinal structures and achieving intraoperative hemostasis is delivered via an optical fiber connected to a thulium laser generator (SRM-T2F, Raykeen, Shanghai, China).

Both the instruments and their respective actuation units are mounted onto the rigid robotic arm (Figure 1 (C)). Each instrument is designed as a modular assembly consisting of an actuation component and an interchangeable instrument component, a configuration that facilitates rapid assembly and disassembly (Movie S1). The three actuators are conically arranged to integrate tip-mounted tools. Figure 1 (D) shows the instruments' distal section and the guiding trocar. The trocar integrates six channels: three for steerable instruments (steerable endoscopic camera, gripper, laser

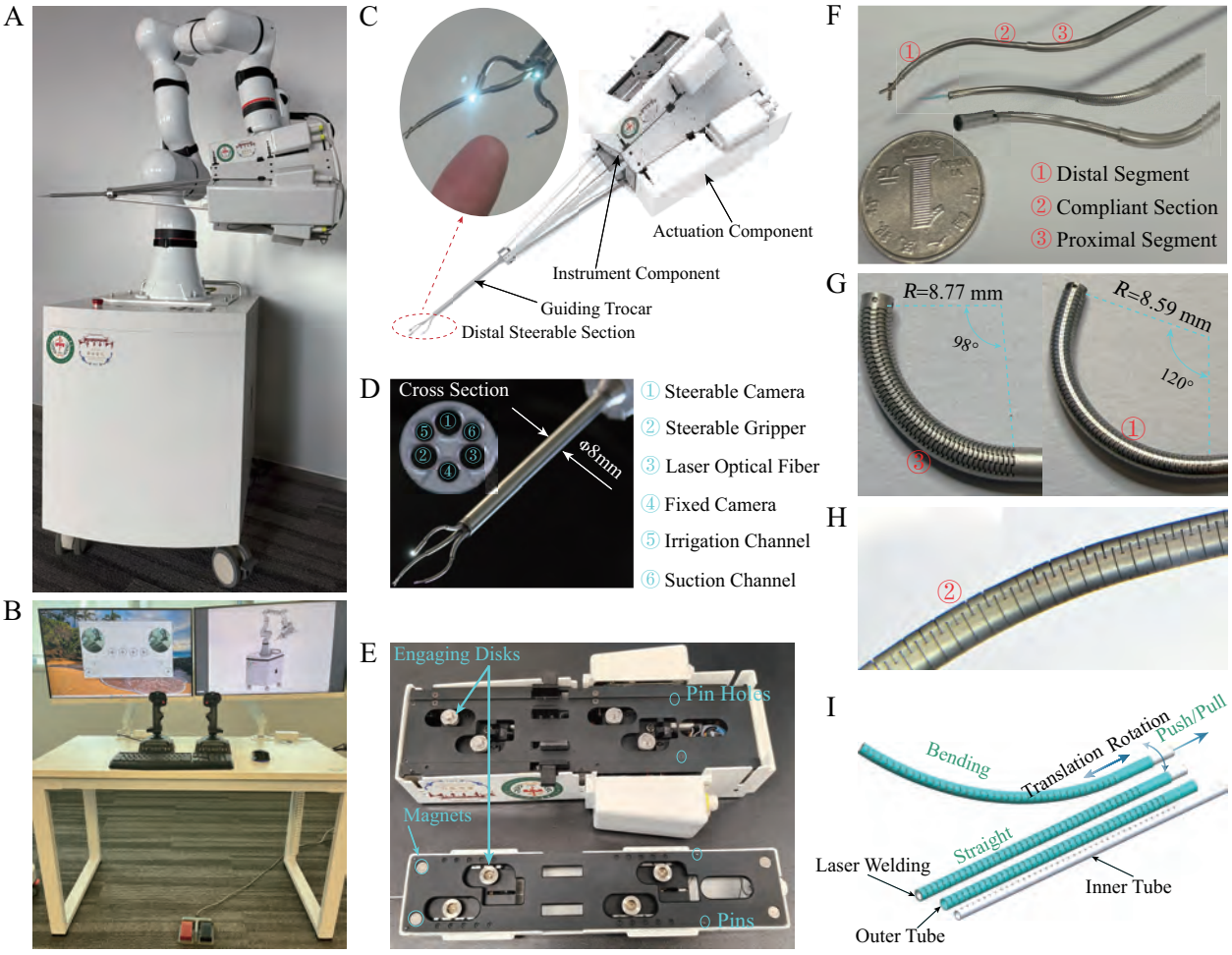

Figure 1. **Robotic system designed for minimally invasive anterior lumbar nerve decompression.** (A) Bedside robot. The robotized instruments and actuation unit are mounted on a rigid robotic arm. (B) Surgeon control console. Surgeons manipulate two joysticks to control instruments, with endoscopic views displayed on screens. (C) Actuation unit for the instruments and the guiding trocar, supporting rapid instrument component release and assembly. (D) Steerable sections of instruments and the guiding trocar, featuring six specialized channels for instruments and saline circulation. (E) Detached instrument components and actuation components. (F) Steerable segments of the dual-segment architecture. (G) Tenon-mortise slits of the steerable segment. (H) Passive compliant section featuring 'I'-shaped slits. (I) Schematic representation of the CPPR-based steerable segment. Each segment is formed by two concentric hollow steel tubes, facilitating the integration of a secondary segment or tip tool; this dual-segment design provides enhanced dexterity and an expanded operational workspace.

fiber), two for saline irrigation/suction, and one for a fixed endoscopic camera. The steerable camera provides surgical site visualization, and the fixed camera monitors instruments' shape. A saline-filled environment is essential for cleaning and cooling the surgical field, so the irrigation and suction channels create a saline circulation loop. The trocar has been miniaturized to an outer diameter (OD) of 8 mm and an inner diameter (ID) of 7.6 mm, facilitating a small percutaneous incision to access the vertebral bodies. The steerable sections of the instruments are able to retract fully within the trocar or extend as required for surgical manipulation. Each instrument comprises a dual-segment CPPR arm (Figure S9) with an integrated tip tool: an endoscopic camera (OVM6946, Omnivision, USA), a gripper (GM-FB-C-N-10-1200, Grit, China), or a thulium laser fiber (Raykeen-365-300, Raykeen, China). The 0.9 mm hollow lumen of each CPPR instrument provides sufficient space to accommodate the camera signal wire (0.6 mm), the gripper actuation wire (0.5 mm), and the laser fiber (0.365 mm).

Pins and magnets are integrated at the interface between the instrument component and actuation component (Figure 1 (E)) to ensure precise alignment of transmission disks. All electric motors (ECU16036H12-S108, MOONS', China) are housed in the actuation component, with engaging disks transmitting motion to the instrument component (Figure S11 (B)). The structure of the robotized steerable instruments is inspired from a concentric push-pull robot arm (CPPR) architecture. As illustrated in Figure 1 (F), the distal segment passes through the hollow lumen of the proximal segment via the thin-walled CPPR structure. A passive compliant segment featuring 'I'-shaped slits is integrated into the distal segment, facilitating smooth sliding within the proximal segment. The specific configurations of the steerable and compliant segments are detailed in Figure 1 (G) and (H), and the geometric parameters of the tubes are listed in Table S1. A single steerable segment consists of two concentric hollow steel tubes featuring symmetrically aligned patterned slits, which are fixed at the distal tip through laser welding (Figure 1 (I)). The relative axial pushing or pulling of the inner tube deforms the steerable segment, thereby enabling 2D arc bending. By integrating rotational and translational DoFs (Figure 1 (I)), each segment achieves 3 DoFs (bending, rotation and translation). This configuration allows all instruments to be controlled either individually or in coordination to achieve precise tip positioning. Figure S11 (A) and (B) illustrate the core actuation mechanism of a single segment, with a spline-thread shaft connected to the inner tube. Rotation of two gears enables segment bending or rotation. Furthermore, the instrument components are

secured to the actuation unit via specialized locks and grooves, and quick-release buttons enable the rapid replacement of instruments (Movie S1).

Single-Arm Performance Evaluation

The maximum bending angles of the proximal and distal segments reach 98° and 120°, respectively (Figure 1 (G)). With a maximum relative translation distance of 10 mm, the tip tool can achieve various poses (Figure 2 (A)). The end effector of one dual-segment arm provides a workspace of approximately 72.66 cm^3 (Figure 2 (B)), even when the translation DoF of the proximal segment is deactivated. A 120° field-of-view endoscopic camera at the tip provides surgeons with a expansive surgical view.

Motion accuracy is paramount for surgical safety and is intrinsically linked to both mechanical precision and the efficacy of the kinematic model. We developed an optimization-based inverse kinematics model to calculate actuation inputs for target tip positions. To evaluate its performance, the robotic arm followed a series of 2D paths, designated as 'WCHSCU', each of which consists of 360 discrete points. As shown in Figure 2 (C) and Movie S2, both segments bent and translated simultaneously, guiding the tip position marker along the path points. Repeatability was further validated using identical 'C' paths, and a spiral path was employed for 3D path-following evaluation. Position errors between the desired and actual paths are shown in Figure S2, with a maximum error of 1.65 mm and a root-mean-square error (RMSE) of 0.9 mm under open-loop control. The maximum error occurred at the 'W' path due to sharp turning points. When following the smooth 'C' path, the RMSE and maximum error were reduced to 0.85 mm and 1.1 mm, respectively. Throughout these experiments, the velocity of the marker was consistently maintained at approximately 9 mm/s. The error sources include mechanical assembly imperfections, measurement inaccuracy from the optical sensing system (OP-M620, AIMOOE, China), and inertial effect at sharp turning path points. In addition, the axial elasticity of the passive compliant section (exhibits spring-like behavior) results in an actual push/pull displacement at the steerable section that is smaller than the commanded configuration, thereby introducing kinematic inaccuracies. Reducing velocity to around 4 mm/s improved path 'W' performance, yielding an RMSE of 0.88 mm and a maximum error of 1.3 mm. Although limited lumen space precludes the integration of tip-mounted internal

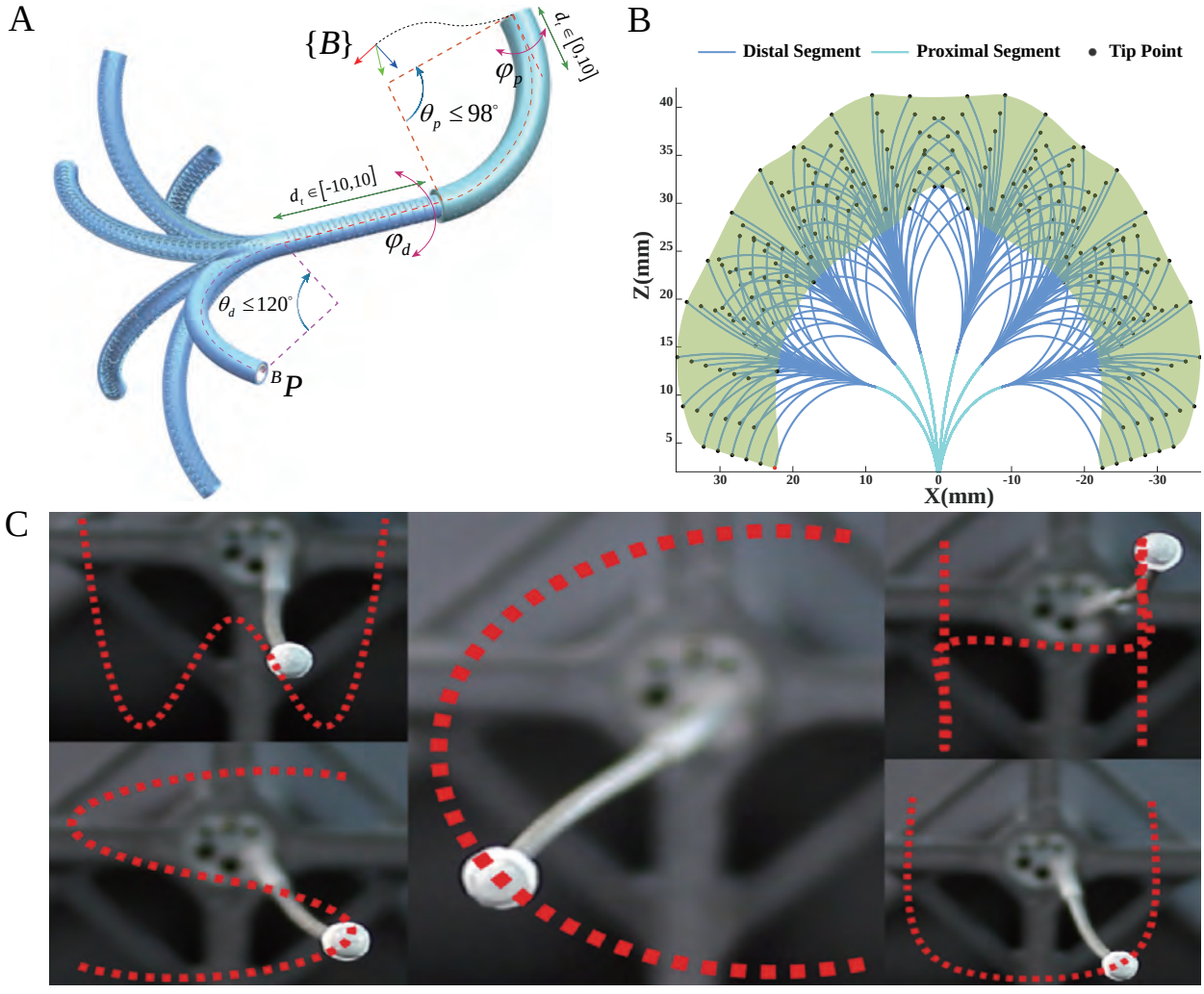

Figure 2. **Tests on the robot's basic performance, including coverage of workspace and following given paths.** (A) Parameterized robot arm shape. The distal segment passes through the hollow lumen of the proximal segment, enabling high dexterity with large bending angles. (B) Cross section of the end-effector workspace with the translation DoF of the proximal segment deactivated. (C) Open-loop 2D path following.

sensors for closed-loop control, the current open-loop path-following accuracy is deemed feasible for resecting degenerative spinal structures, as surgeons can effectively utilize real-time endoscopic visual feedback for instrument guidance.

Stiffness is a critical performance metric directly affecting surgical maneuverability. Therefore, we systematically evaluated the stiffness of both robotic segments. The steerable segment was connected to a force sensor (SBT641, SIMBATUOCH, China) via a steel wire. As shown in Figure 3 (A), the outer tube was secured in a fixed position, and a linear stage applied displacement to the inner tube to generate relative push/pull distance. The distal segment's passive compliant segment was clamped to eliminate compliance effects. The inner tube push distance served as the independent variable, with the corresponding tip force recorded as the experimental output. Figure 3 (B) presents the measured force across a push distance ranging from 0 mm to 4 mm, with an increment of 0.1 mm. As a result, the maximum tip forces generated by the proximal and distal segments were 4.4 N and 2.6 N, respectively, sufficient for manipulating most elastic biological tissues. Additionally, a 100 g weight was hung at the tips of the two segments to evaluate their payload-carrying capability. Key snapshots of this process are shown in Figures 3 (C) and (D), with the full motion documented in Movie S2. Both segments successfully lifted the weight, with the distal segment achieving a 5 mm maximum push distance due to its slender body and lower structural stiffness. Although the material is stainless steel and each segment has a wall thickness of 0.1 mm, the stiffness increased notably with the increase of bending angle. This phenomenon results from the tenon-mortise slit design, where larger bending angles facilitate mechanical interlocking between the tenons and mortises. Peak stiffness is achieved once all tenon-mortise slits are fully interlocked.

Beyond testing the stiffness of the two segments individually, we also evaluated the stiffness of the dual-segment robotic arm (Figure S3 (A)). The distal segment tip interacted with the force sensor, with a 3 mm push distance applied to the proximal segment. The translational DoF of the distal segment was varied across four settings ($d_t = [-6, -3, 3, 6]$ mm), and the resulting tip force was measured for each configuration. Predictably, extending the passive compliant segment from the proximal segment ($d_t = [3, 6]$ mm) reduces the recorded tip force, whereas retracting it ($d_t = [-3, -6]$ mm) leads to a measurable increase in force. The physical interaction between the robotic arm and the force sensor is illustrated in Figure S3 (B), with a comparative analysis of the

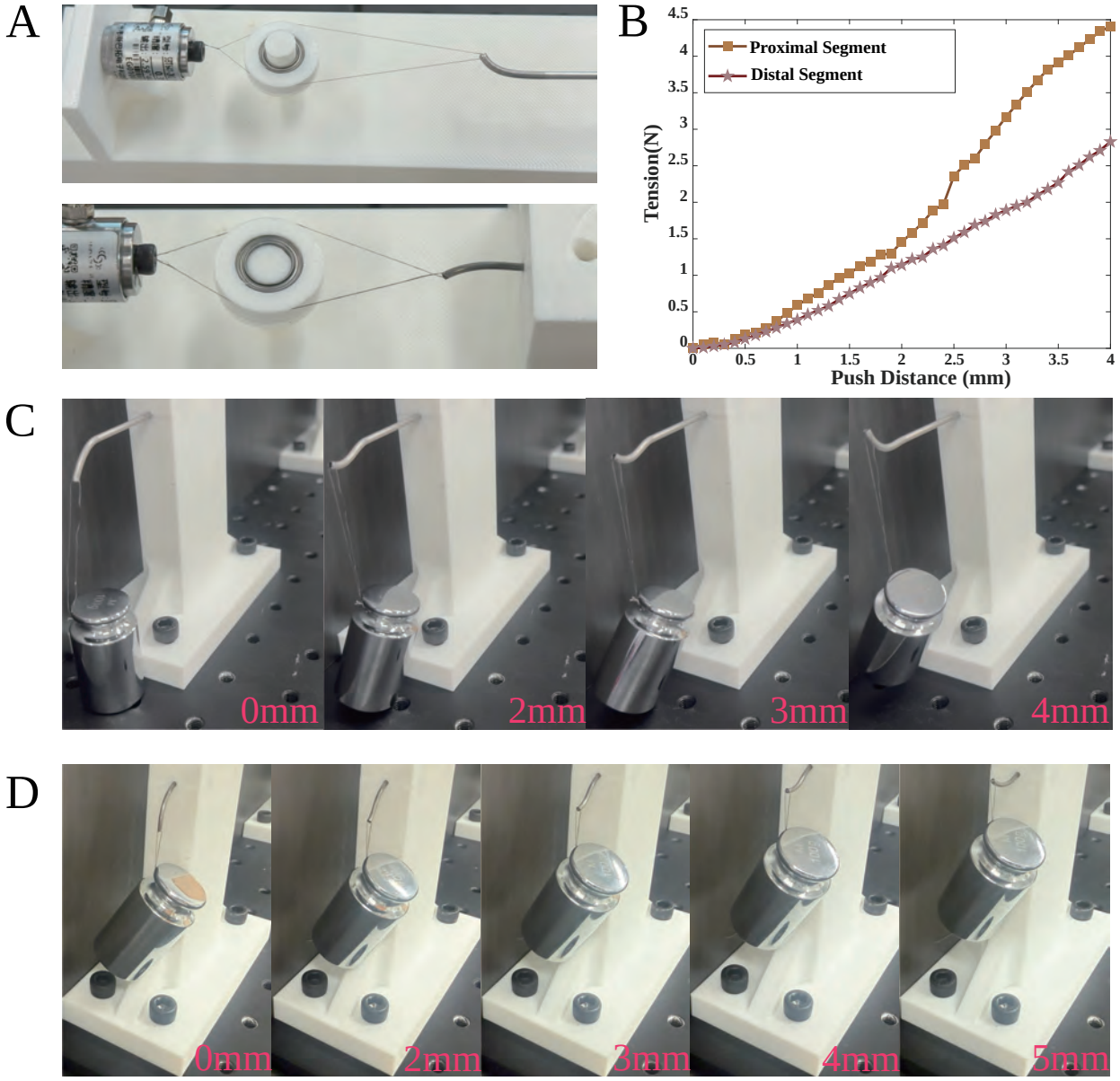

Figure 3. **Single-segment stiffness testing.** (A) Tension testing setup. The tip of steerable section connects with a force gauge using a wire and a pulley. (B) Tension with various push distances acted on the inner tube. (C)/(D) The proximal/distal segment is dragging a 100g weight, and the distance value at the bottom right of each snapshot is the push distance applied on the inner tube.

forces under these four configurations presented in Figure S3 (C). At the settings of d_t = 3 mm and 6 mm, the interaction force exhibited a slight increase relative to the push distance, accompanied by visible deformation of the compliant segment (highlighted by dashed elliptical circles in Figure S3 (B) - (iii) and (iv)), yielding a maximum tip force of approximately 0.2 N. Conversely, when the passive compliant section was retracted into the proximal segment, the interaction force rose obviously as the push distance varied from 2 mm to 4 mm. Specifically, in the configuration where $d_t = -6$ mm and the push distance was 4 mm, the interaction force reached 0.658 N, with both segments maintaining an arch shape (Figure S3 (B) - (i) and (ii)). This confirms that tip manipulation force can be regulated by adjusting translation distance d_t. Such a mechanism allows for high-stiffness configurations suitable for manipulating elastic intervertebral disc, and low-stiffness configurations can be selected for nerve nerve dissection. Furthermore, the proximal segment's translational DoF ensures the maintenance of an expansive workspace even when the distal segment is in a retracted state.

To quantify payload resistance, we attached a position marker to the arm tip and measured tip deviation between load-free and loaded conditions. As shown in Figure S3 (D), a single proximal segment was initially evaluated. We sequentially set the push distance acting on the inner tube to 1 mm, 2 mm and 3 mm, and loads of 20 g and 50 g were respectively hung at the tip. Under the identical actuation settings, a smaller deviation of the tip position between in load-free and with-load scenarios indicates a higher structural stiffness. The recorded deviations are detailed in Table S4. For the single proximal segment, the tip deviation decreased as the push distance increased, demonstrating that the tenon-mortise slits gradually interlocked to enhance structural rigidity. Notably, the deviation was only 2.12 mm whereas the load was 50 g and the push distance was 3 mm, showing the high stiffness of the proximal segment. Similar tests were conducted on the dual-segment robotic arm with the distal segment fully extended from the proximal segment. Due to the extended cantilever length and the inherent flexibility of the distal segment (dominated by the passive compliant section), the tip marker exhibited downward deflection (Figure S3 (D)). The tip deviations for various distal segment actuation configurations is listed in Table S4. Although the load was 50 g and the bending angle in load-free condition reached around 70°, the maximum deviation was 16.8 mm. Correspondingly, an increase of push distance brings the weight move upwards. In summary, as the single proximal segment provides the high stiffness necessary to

withstand external forces, the dual-segment configuration exhibits controlled compliance under external payloads.

In addition, a conventional square-slit CPPR arm was developed to compare the ability of withstanding load with the tenon-mortise design, maintaining identical cross-sectional cut area, slit width, slit count, and gap distance. A 50g load was also applied at the tip and the inner tube was respectively actuated with a push distances of 1 mm, 2 mm and 3 mm. Initially, the load was exerted in the bending plane (radial load, as illustrated in Figure S10 (A)). At a 1 mm push distance, the square-slit design exhibited limited ability to withstand the load, and the increase of push distance failed to mitigate the shape deformation. In contrast, the tenon-mortise design demonstrated superior structural stability under load (Figure S4 (A)). Subsequent tests involved applying a lateral load to the side of the arm (Figure S10 (A)). As a result, the square-slit design proved inadequate in withstanding lateral forces (Figure S4 (B)). Bending snapshots presented in Figure S4 (C) confirm that no interlocking occurs in the square-slit design, thereby validating the mechanical advantages of the tenon-mortise architecture. Since the internal slits of the inner tube remain invisible during physical testing, Finite Element Method (FEM) analysis was employed to investigate the deformed shape of the tenon-mortise design and verify simultaneous interlocking across both tubes. The analysis result, shown in Figure S4 (D), indicate that the redundant interlocking mechanism enhances both torsional rigidity and flexural stiffness, as the second moment of inertia of the tube increases upon interlocking. Conversely, a lot of vacant space within the square-slit design results in a relatively lower second moment of inertia, compromising its overall stiffness.

Robot Arm Coordination

The maneuverability of the robotized instruments was assessed, focusing on the visual field and multi-arm coordination. As shown in Figure S5 (A), the instruments performed tasks inside a narrow constrained workspace where four small rubber rings were arranged for manipulation. The entire robotic system was required to complete three sequential objectives: the gripper arm picks up the green rubber ring and places it in a semi-closed corner (highlighted by the green arrow in Figure S5 (A)); the gripper arm subsequently picks up the red, black and blue rubber rings to hang

them in the laser optical fiber arm; the gripper arm retrieves the three rubber rings and places them onto three protruding columns in sequence.

During the execution phase, the operator first positioned the trocar using the rigid robotic arm and subsequently activated only the slender instruments for task performance. Figure S5 shows key motion snapshots of instrument's motion. Throughout the procedure, the operator relied exclusively on real-time visual feedback provided by the two endoscopic cameras. To maintain a comprehensive view of the core manipulation area, the operator maneuvered the gripper arm and simultaneously controlled the steerable camera (Movie S3). The steerable camera arm was initially extended from the trocar channel to capture a comprehensive view of the entire task space (Figure S5 (B)). Then, the laser arm and the gripper arm reached the task space (Figure S5 (C)), with the laser arm moving aside to clear the operational field for the gripper. As shown in Figure S5 (D) and (E), the gripper arm successfully retrieved the green rubber ring and placed it within a semi-closed corner measuring only $3 \times 3 \times 3$ mm. Next, the operator coordinated the two instruments to collect the remaining three rings and hang them on the laser optical fiber arm, a process that required inter-arm coordination (Figure S5 (F) and (G)). During this step, the pose of the steerable camera was continuously adjusted to ensure the manipulation area remained visible. Finally, the gripper arm retrieved the three rubber rings from the laser arm (Figure S5 (H)) and transferred them to the three protruding columns (Figure S5 (I)). The entire coordination sequence was completed within approximately 3 minutes, as documented in Movie S3. It is anticipated that task efficiency can be further enhanced by upgrading the surgeon-robot interface.

Surgical Protocol of Robot-assisted Anterior Decompression

The distinctive advantage of the MicroSpine reside in the slenderness, dexterity, structural stiffness and effective multi-arm coordination of its robotic instruments. Leveraging these integrated features, we propose a robot-assisted minimally invasive anterior decompression protocol, which follows standard OLIF steps, and the key difference in the decompression procedure.

The surgeon makes a small oblique abdominal incision whilst the patient's body is in the right lateral decubitus position (Figure 4 (A)). A retractor is subsequently advanced through this percutaneous port to the anterior side of the spine, during which the surgeon delicately moves

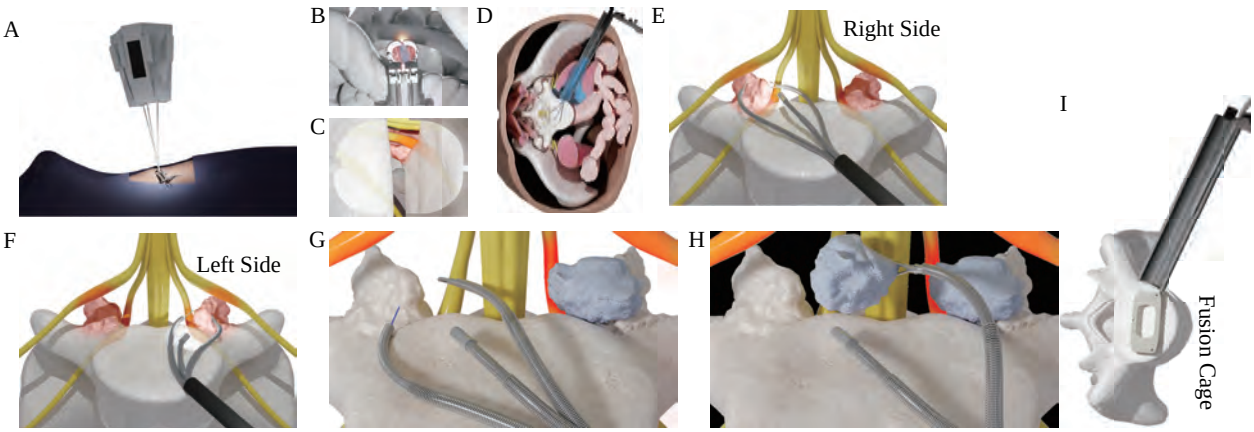

Figure 4. **Robot-assisted surgical protocol for anterior minimally invasive decompression.** (A) The trocar is advanced through the anatomical corridor connecting the incision port to the vertebral body. (B) Initial limited visualization of the vertebra following the establishment of the surgical corridor. (C) Resection of the intervertebral disc by the thulium laser fiber, exposing the posterior spinal area. (D) Saline irrigation of the surgical site to facilitate laser resection and maintain endoscopic camera clarity. (E) Simultaneous deployment of the three robotic instruments at the right posterior spinal region for osteophyte resection. (F) Precise instrumentation control enabling access to the left posterior area, allowing for the treatment of central posterior stenosis. (G) Nerve root retraction using the gripper to mitigate the risk of iatrogenic injury during decompression. (H) Successful retrieval of resected degenerative tissue by the gripper. (I) Manual implantation of the fusion cage to restore spinal stability following the decompression procedure.

aside the ureters and aorta to minimize the risk of iatrogenic trauma. To establish a stable surgical corridor (Figure 4 (B)), a screw is secured to the vertebra via the retractor, which is then fixed to the operating bed. Once the surgical corridor is established, the herniated disc is visualized, and an access port is created within the intervertebral disc to accommodate the robotic instruments. The rigid robotic arm advances the trocar through the corridor, and the laser arm resects the intervertebral disc under dual-endoscopic guidance (Figure 4 (C)). In the resection process, the saline irrigation and suction pumps work simultaneously to maintain a saline-filled circulation environment, which serves to evacuate surgical effluent and ensure the continuous clarity of the endoscopic cameras. The instruments are then advanced toward the posterior area of the spine to resect right-sided articular process osteophytes using the thulium laser. Throughout this process, surrounding nerves are meticulously dissected and protected by the gripper to prevent unintentional trauma (Figure 4 (E)).

The instruments are subsequently navigated to the left posterior area which is typically inaccessible via standard OLIF. The thulium laser addresses central stenosis during the transition (Figure 4 (F)). Decompression is completed by resecting the left articular process osteophytes. The steerable camera is strategically positioned to maintain comprehensive visualization of the surgical site and also preserves the necessary operational space for the manipulation instruments. The gripper is utilized to retract nerve roots, preventing iatrogenic injury (Figure 4 (G)), and to remove the resected osteophytes (Figure 4 (H)). Finally, instruments are withdrawn, and the surgeon manually performs interbody fusion cage implantation to retore spinal stability (Figure 4 (I)).

In summary, standard OLIF procedures typically accommodate only one or two surgical tools within the constricted intervertebral disc space. In contrast, the slender and highly dexterous instruments facilitate the simultaneous resection of degenerative tissues in both the anterior and posterior spinal regions, including the complex anatomical structures of the bilateral articular process joints. The non-contact thulium laser beam provides precise tissue resection, and the laser arm itself can be utilized to retract soft tissues and nerves. Furthermore, the standard vertebral retractor utilized in this protocol provides sufficient fixation and dilation of the surgical site, thereby eliminating the necessity for additional specialized fixators for the MicroSpine system.

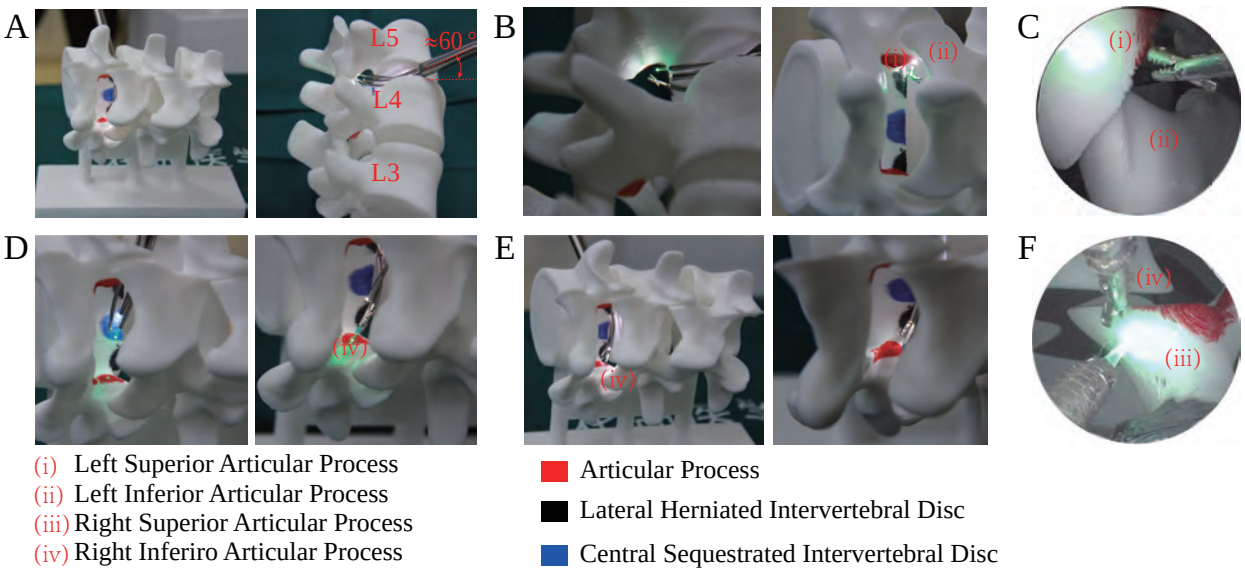

Figure 5. **Accessibility validation within a 3D-printed human vertebral phantom model.** (A) Experimental setup and side view illustrating the positional relationship between the vertebrae and the robotic trocar. (B) Simultaneous deployment of the three robotic instruments at the left articular processes to simulate osteophyte resection. (C) Endoscopic visualization of superior and inferior articular on the left side. (D) Precise instrumentation control as the system approaches the right posterior region. (E) Side view and close-up detail of instruments positioned at the right superior articular process. (F) Endoscopic view of manipulating the right superior and inferior articular processes.

In Vitro Test on a 3D-Printed Human Vertebral Phantom Model

The accessibility of key surgical sites and the coordination of the three instruments within the constricted vertebral space were first evaluated using a 3D-printed human vertebral phantom model. This physical phantom model was reconstructed from Computed Tomography (CT) scanning data of a patient, focusing on the L3–L5 lumbar vertebrae. As shown in Figure 5 (A), the superior articular process, herniated parts of the intervertebral disc and the central sequestrated intervertebral disc are labeled in red, black and blue, respectively. The laser arm was utilized to sequentially approach these targets under real-time visualization provided by the steerable endoscope, and green laser light was employed to simulate resection and validate reachability. Subsequently, the rigid arm advanced the trocar along the axial direction. As the trocar reached the anterior aspect of the

disc space, the slender instruments entered the intervertebral space, providing a rigorous test of their dexterity and performance under conditions simulating severe intervertebral disc stenosis. As the trocar reached the anterior side of the intervertebral disc space between L4 and L5, the slender instruments entered the intervertebral disc space, fully testing the instruments' dexterity and simulating conditions associated with intervertebral disc stenosis. Visibility, accessibility, and maneuverability were validated across six critical surgical zones: the left superior and inferior articular processes, the posterior midline of the L5 and L4 vertebrae, and the right superior and inferior articular processes. The initial target was the left superior articular process, a region notably challenging to access during standard OLIF (Figure 5 (B)). All three instruments successfully navigated the left herniated intervertebral disc, confirming the laser arm's capacity to establish a path to the posterior region via the dexterous robotic architecture. The endoscope maintained a view of the target site (Figure 5 (C)), and the gripper's distal segment successfully rotated toward the left inferior articular process, demonstrating notable dexterity for posterior access.

The instruments were subsequently controlled to reach the right side of the posterior area for further accessibility testing. The robotic instruments successfully crossed the spinal canal at the L5 posterior midline to reach the right superior articular process (Figure 5 (C)). The orientation of motion was confirmed by the green light emitted from the laser optical fiber (Figure 5 (D)). By delicately adjusting the poses of the two manipulation instruments (the laser optical fiber and gripper), both the laser fiber and the gripper successfully reached the right superior and inferior articular processes (Figure 5 (E)) under continuous endoscopic visualization (Figure 5 (F)). The result also indicated that the instruments passed the midline of vertebra L4. Similarly, the distal segments of the two manipulation arms were adjusted to bend beside the right inferior articular process, allowing the instruments to successfully reach all six the target areas.

Across 20 repeated trials, the success rates for reachability were 100% for the left posterior region and 95% for the right posterior region. The single failure occurred during the initial trial when the laser arm was incorrectly operated due to inaccurate anatomy recognition; all subsequent trials were performed successfully. Navigating the tortuous articular processes on the left side required the robotic segments to achieve relatively large bending angles. Specifically, the proximal and distal segments of the gripper arm reached angles of approximately 50° and 70°, respectively, both of which remained within their maximum operational limits (Figure 5 (B)). For observing the

instruments' shape, the OLIF retractor was not utilized in this experiment, meaning the intervertebral disc space remained unexpanded. Given that the patient-derived CT data showed an intervertebral distance of only approximately 6 mm, the proximal segments of the three instruments operated in extremely close proximity to one another. In clinical practice, surgeons typically utilize retractors to dilate this space, especially when addressing spinal stenosis. These results collectively validate the system's robust capability to navigate confined and complex spinal anatomy.

In Vivo Animal Experiment

Given the paucity of clinical experience regarding the use of lasers for lumbar nerve decompression, the precise calibration of the thulium laser generator's operational parameters is imperative. These settings must be meticulously adapted to enable various surgical maneuvers, including the resection of elastic fibrous rings, nucleus pulposus, and dense osseous structures, as well as the cauterization of venous vessels for intraoperative hemostasis. To rigorously evaluate the overall performance of the robotic system, we conducted validation using a porcine spine, focusing specifically on the surgical efficacy of the robotic instruments.

The pig was anesthetized and secured on the operating bed in a position aligned with standard OLIF procedures (Figure 6 (A) and Figure S6). The surgeon established a surgical corridor to the anterior side of the lumbar vertebrae using a small oblique abdominal incision and a lateral retractor (OLIF25^{TM}, Medtronic, USA). Under comprehensive endoscopic guidance, the surgeon manipulated the robotic trocar via joysticks (Movie S4). To optimize visualization and facilitate hemostasis, saline was irrigated into the L4–L5 disc space, with simultaneous suction deployed for the continuous removal of debris. Upon instrument extension, the steerable camera was adjusted to visualize the targeted resection area (Figure 6 (B)). To identify the optimal laser configurations, including power and pulse energy, we initially utilized a setting of 2 J (pulse energy) and 20 W (power). However, these parameters proved insufficient for the resection of tough fibrous tissue, necessitating an adjustment to 4 J and 40 W. With these refined settings, the laser effectively resected the fibrous ring, with tissue fragments observed floating within the saline environment (Figure 6 (B)-(i) and Movie S4). During the procedure, transient bleeding was observed (Figure 6 (C)-(ii)), which momentarily compromised visual clarity. In standard OLIF, surgeons typically use

electrocoagulation to manage bleeding. Our system leverages the thulium laser for venous cauterization by employing differentiated parameter settings. The finalized hemostasis configuration (2 J and 20 W) effectively cauterized the veins without causing thermal damage to adjacent nerves or fibrous tissues. Integrated saline circulation successfully evacuated the turbid fluid, restoring surgical site visibility. Because the hemorrhage was managed immediately without requiring instrument exchange, the bleeding episode lasted only approximately 10 seconds, with an estimated total intraoperative blood loss of merely 5 mL.

After hemostasis, the laser continued to resect the intervertebral disc to establish a passage to the posterior AREA. Figure 6 (D) shows endoscopic visualization of nucleus pulposus resection, which is characterized by a softer consistency than the fibrous ring. The total duration for full intervertebral disc resection was approximately 90 seconds, notably shorter than the 5 minutes typically required in standard OLIF due to the avoidance of frequent instrument exchange and endoscope cleaning. The thulium laser enables simultaneous resection and hemostasis, with saline circulation removing resected tissue. In this step, coordinated multi-arm manipulation enhanced overall efficiency. The gripper arm was utilized to retract resected tissue, thereby clearing the laser's operational path (Figure 6 (E)). Once the anterior-posterior passage was established, the instruments were paused for 20 seconds to fully clear the surgical field before advancing to the posterior area. Laser parameters were subsequently adjusted to 4 J and 60 W for the resection of the articular processes. The laser successfully resected the right superior and inferior articular processes within approximately 2 minutes (Figure 6 (F)), and the gripper arm provided assistance by retracting floating tissues.

This in vivo animal experiment validates the thulium laser as a versatile and precise tool for both lumbar decompression and hemostasis. Since the basic structure of porcine spine differs from that of human (the height of intervertebral disc in lumbar is only around 3 mm (*51*)), there is almost no space to enter the left side of the posterior area. In this experiment, the effectiveness of resecting intervertebral disc, hemostasis and multi-arm coordination has been evaluated. Due to the narrow space of porcine spine, we did not mount the gripper at the tip of one robot arm, which only worked as a stripper. Through tuning the parameters of the laser beam, we found that although the system provides precision in resecting tissues, it only covers a small area of tissue. Therefore, the distal dexterity of robotic instruments is necessary to bring the laser to a series of the desired targets. The

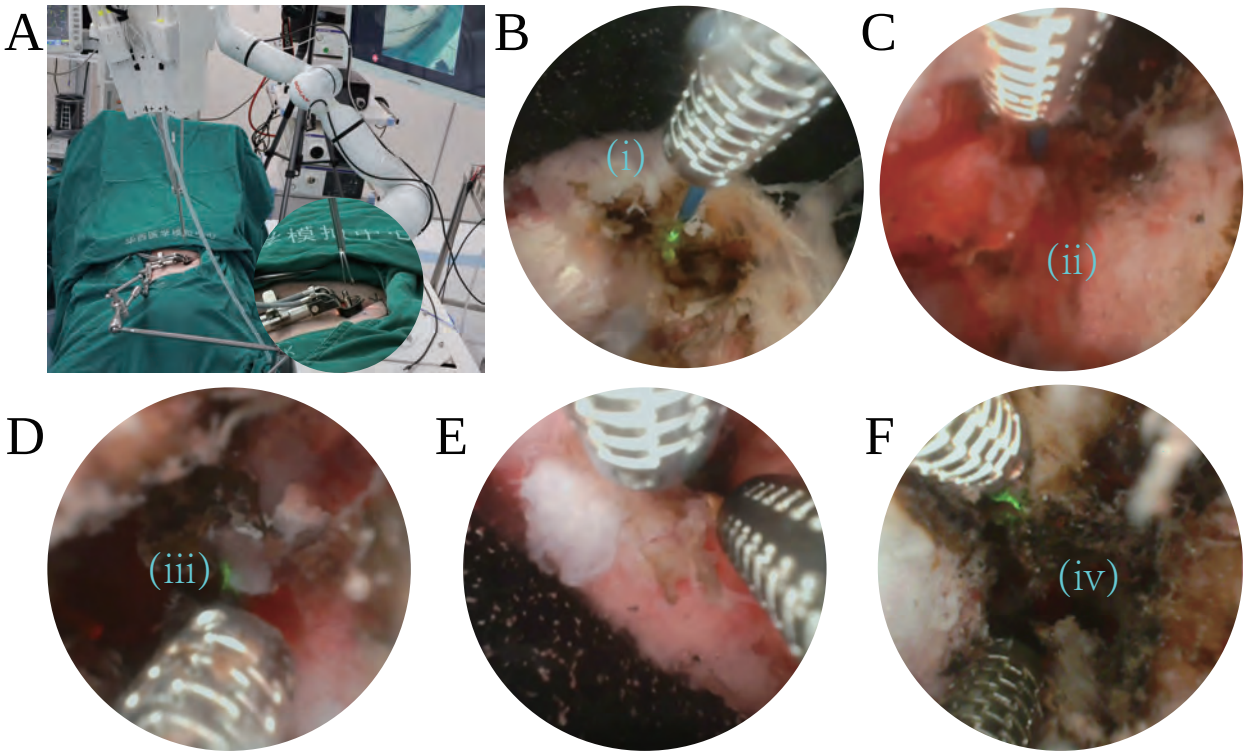

Figure 6. **Evaluation of the robotic system in an in vivo porcine spinal structure, focusing on surgical tool functionality and accessibility to a series of targets.** (A) The anesthetized pig is in the lateral decubitus position; the rigid robotic arm aligns the trocar with the standard OLIF retractor. (B) Initiating an opening of the fibrous ring. (C) Management of intraoperative bleeding via irrigation and suction to restore visual field clarity. (D) Resection of the nucleus pulposus to establish access to the posterior spinal area. (E) Coordinated manipulation of tissues using two robotic instruments. (F) Laser-assisted resection of the right posterior superior articular process.

success of testing on porcine spine also demonstrates the notable accessibility of the slender and dexterous robotic instruments.

Human Cadaver Tests

To further evaluate the clinical feasibility and anatomical adaptability of the MicroSpine system in a human context, we conducted human cadaver tests (Figure 7). The specimen was secured in the right lateral decubitus position on the operating bed. Following the standard OLIF clinical pathway, the surgeon made a skin incision of approximately 3 cm in length, stripping the muscle until the intervertebral disc (between vertebrae L3 and L4) was fully exposed (Figure 7 (A) and Figure S7). A guidewire was inserted into the disc, and Cone Beam CT (OEC 3D Supreme, GE Healthcare, USA) confirmed surgical targets (Figure S8 (A)).

Next, the lateral retractor was placed and fixed on the operating bed, dilating a disc space of approximately 8 mm between the two vertebrae for the three robotic instruments. A 7×16 mm access port was manually created at the disc (Figure 7 (B)). The depth of the incision on the intervertebral disc was only around 2 mm (Figure S8 (B) and (C)). The rigid robotic arm was then employed to navigate the trocar through the retroperitoneal space, ensuring it was aligned to the target disc (Movie S5).

Upon the trocar reaching the anterior disc space, the three slender instruments were extended into the intervertebral corridor. Saline was irrigated into the surgical site to create a saline-filled environment. The steerable endoscope provided real-time visualization of the intervertebral disc space (Figure 7 (C)). The laser instrument (parameters setting: 4 J and 40 W) was first utilized to resect the intervertebral disc, creating a dedicated passage to the posterior region. After approximately 2 minutes, the intervertebral disc was fully resected, and the steerable camera passed through the passage to visualize the posterior area (Figure 7 (D)). Next, the three robotic instruments were navigated toward the posterior spinal canal to perform bilateral decompression.

The laser arm and gripper arm subsequently began to expose the superior and inferior articular processes (Figure 7 (E)-(i)). The laser parameters were adjusted to 4 Joules and 60 W for resecting the superior and inferior articular processes (Figure 7 (E)-(ii)). To confirm that the instruments reached the target surgical site, fluoroscopic images were utilized to localize the instruments within

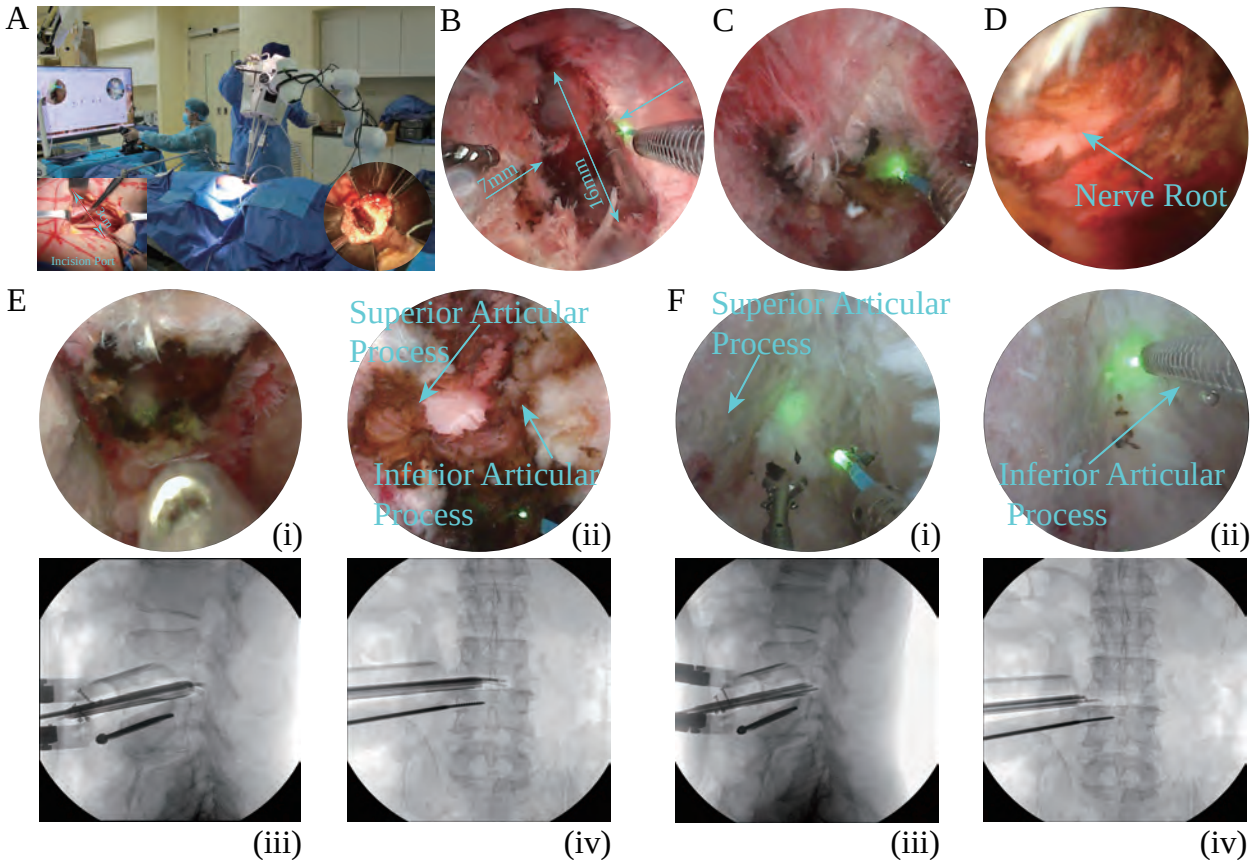

Figure 7. **Human cadaveric evaluation of the MicroSpine system.** (A) Human cadaver positioned in the lateral decubitus position, with the robotic trocar aligned. (B) Surgeon incised a small port on the intervertebral disc to label the entrance for the instruments. (C) Endoscopic visualization of the robotic instruments as they enter the intervertebral disc space. (D) Steerable camera arm passed through the small passage on the intervertebral disc to collect the view of posterior area. (E) Decompression at the right side of the posterior area. (E-i) Resecting elastic tissue around the right side of superior and inferior process. (E-ii) The laser beam was resecting the hard spine tissues. (E-iii)/(E-iv) Lateral/frontal fluoroscopic images of the instruments on the right side. (F) Decompression at the left side. (F-i)/(F-ii) Endoscopic visualization of the laser arm resecting the superior/inferior articular processes. (F-iii)/(F-iv) Lateral/frontal fluoroscopic images of the robotic instruments at the left side.

the spine (Figure 7 (E)-(iii) and (iv)). The laser arm was then directed to resect the two articular processes, completing the resection within just 80 seconds (Movie S5).

The three instruments then navigated to the superior and inferior articular processes on the left side. Similarly, the two manipulation instruments reached the target area (Figure 7 (F)), and their positions within the spinal structure were also confirmed using fluoroscopic images (Figure 7 (F)-(iii) and (iv)) before resection. In dealing with the articular process (Figure 7 (F)-(i) and (ii)), the gripper arm stripped the tissues and laser beam precisely worked on the hard osseous structure. Finally, the instruments withdrew from the retractor corridor, and the surgeon manually inserted a fusion cage into the intervertebral disc (Figure S7 (B)).

The duration for the steps in the procedure were as follows: 3 minutes for resecting the intevertebral disc, 1 minute for resecting the articular process on the right side, 3 minutes for moving to the left side, and 5 minutes for resecting the articular process on the left side. The entire decompression procedure, from resecting the intervertebral body to withdrawing the trocar from the retractor, took approximately 15 minutes. Much of this time was spent confirming the surgical target using the CBCT machine. It should be noted that the human cadaver was not diagnosed with degenerative spinal disease, and bleeding issue was not observed because the cadaver had been stored in refrigerator for more than one year. The success of effectively reaching the tortuous posterior area and resection also demonstrates the clinical value. The instruments' dexterity and large workspace enable resection of degenerative tissues in both the intervertebral disc and posterior spinal areas.

Discussion

In this study, motivated by the limitations of available instruments in standard oblique lateral interbody fusion (OLIF) surgery, we designed the robotic system MicroSpine to enhance the surgical outcome of lumbar nerve decompression. This technique leverages the natural anatomical corridor and minimal invasiveness of OLIF and also overcomes its inherent shortcomings related to the inability in accessing posterior areas via an anterior route. The slender, dexterous robotic instruments enable direct and complete resection of anterior and posterior degenerative spinal structures, extending access to hypertrophic facet joints and ligamentum flavum—pathologies inaccessible in standard OLIF. Standard OLIF surgery is able to resect the pathological tissues at the anterior

area, and decompress the nerves by dilating a space, leaving the osteophyte at the posterior area unaddressed. Our system transforms OLIF from an indirect decompression technique into a direct decompression strategy, notably expanding its surgical indications. Patients suffering from both anterior and posterior lumbar canal stenosis can now benefit from a complete, minimally invasive anterior approach, potentially reducing iatrogenic trauma, intraoperative blood loss and complications. This robot-assisted OLIF paradigm may represent a meaningful advancement in spinal surgery, particularly for the elderly or high-risk patients who are poor candidates for traditional posterior decompression. Notably, the duration of decompression procedure was reduced to 15 minutes compared to 1-1.5 hours typically required for standard OLIF (*52, 53*). In addition, the blood loss is also reduced compared with standard OLIF. As an estimation, only around 5 mL of intraoperative bleeding will occur in future clinics, because the saline pressure could also minimize bleeding and thulium laser beam could immediately perform hemostasis. More importantly, no iatrogenic trauma occured during the study, which potentially shortens the postoperative hospitalization stay from 1 week (standard OLIF) to 1 day (using MicroSpine).

MicroSpine is inspired by classic multi-arm surgical robots comprising a bedside robot and surgeon control console (*44, 54, 55*). The key features of MicroSpine lie in the robotized instruments and kinematics model. Each instrument has a slender body of 2 mm, 6-DoF dexterity (large bending angle) and maneuverability (withstand radial and lateral payloads). Multi-arm coordination enables effective surgical manipulation. A compact actuation unit enables rotation, bending, and translation DoFs, with an 8 mm miniaturized trocar integrating six channels. A dual-camera system provides comprehensive surgical visualization. This system is specifically designed for lumbar nerve decompression, with potential applications to other orthopedic surgeries.

We combined the advantages of concentric push-pull robotic arms with high-precision laser cutting technology to develop the slender and dexterous robotic instruments. The width of tenon-mortise slits on the stainless steel tube is only 30 micrometers, and the tube wall thickness is 0.1 mm, resulting in a slender arm that leaves a hollow space for the tip tool. This design also allows for ease of actuation, as bending, rotation and translation are integrated at the rear end. The hollow space of CPPR accommodates the endoscopic camera signal wire, actuation wire for gripper's opening/closing and thulium laser optical fiber.

Despite the robotic instrument's slender and hollow design, it maintains relatively high stiffness

in the steerable section due to the tenon-mortise slits. When bending occurs, the tenon and mortise interlock to enhance rigidity. The 'I'-shaped slits in the distal segment passively adapt to the shape of the proximal segment. Because the entire instrument has a translation DoF (Q_p in Figure S12), the distal tool can achieve various poses. This allows the system to adjust the length of extension from the proximal segment (Q_d in Figure S12) to regulate stiffness for nerve/osseous tissue manipulation.

The steerable segment's arched shape enables the piecewise constant curvature assumption for forward kinematics. A nonlinear forward kinematics model was used to develop an optimization-based inverse kinematics model, with a penalty function added to prioritize distal segment motion. Real-time instrument shape estimation enables future surgical navigation integration.

Although the stiffness of the CPPR-based instrument is suitable for handling soft tissues like retracting nerves, it is insufficient for resecting hard pathological degenerative structures. To address this, we integrated a thulium laser optical fiber into the instrument's hollow space to provide the energy necessary for resection. The laser's operation requires a liquid environment, so we incorporated saline irrigation and suction channels in the trocar to establish circulation, which cleans the endoscopic cameras and evacuates effluent. Adjustable laser energy enables both resection and hemostasis.

The evaluation of MicroSpine was systematically organized. One 3D-printed human vertebral phantom model whose CT scanning data was from a real patient diagnosed with spinal degenerative diseases was first used to test the reachability to a series of key surgical targets. Since there was no prior experience in decompressing lumbar nerves with thulium laser, in vivo animal experiment was conducted to further investigate the system's performance, demonstrating its capability to resect intervertebral disc and articular processes in the posterior area. Thulium laser could also be used for hemostasis immediately, which needs no instrument interchange and intraoperative blood loss is reduced. Finally, overall performance was evaluated on a human cadaver, consistent with operations on patients (excluding anesthesia), proving that MicroSpine provides a comprehensive view of the surgical site and enables dexterous surgical manipulation in the target areas.

The system also has some limitations. First, the kinematics model was built based on piecewise constant curvature assumption (*56, 57*), and the shape of the robotic arm does not necessarily follow an arch when faced with external disturbance, which leads to inaccuracy. No internal sensor was integrated in the steerable section due to the limited size of the central hollow lumen, so the

control strategy is open-loop. Accordingly, the surgeon could not obtain haptic feedback in surgical manipulation. Second, the human-machine interaction device is not intuitive for operation, which caused ineffectiveness. Third, the slenderness of the robotic arm also posed challenge to integrate high-quality endoscopic cameras. Currently, the pixel of the endoscopic camera is 400×400, and the focal length is only around 5 mm.

Our future work will focus on developing an intuitive surgeon-robot interface and integrating multimodal large language models (LLMs) to facilitate surgical scene understanding and intraoperative decision support. This will be achieved by fusing preoperative imaging, robotic kinematics, and real-time endoscopic video. For the sensing issue, we will investigate embedding iber Bragg Grating (FBG) sensor (*58*) at the robotic instruments to form a proprioceptive sensing mechanism. As for the endoscopic camera image issues, artificial intelligence model will be developed to enhance the quality and further reconstruct the 3D shape of the surgical site (*59*).

Materials and Methods

Slender Robot Arms Design

The dexterous slender robot arms were designed based on concentric push-pull robot architecture. Each robotic segment comprises two concentric, thin-walled stainless steel (304) tubes permanently fixed at their distal tips. Precision-machined tenon-mortise slits were cut into the steerable section, with the inner and outer tubes assembled at a 180° (Figure S9) phase shift to facilitate antagonistic movement. This configuration enables controlled 2D arc bending through the relative axial translation (pushing or pulling) of the inner tube, which features an extended end for integration with the actuation unit (Figure S9). To ensure smooth mechanical transitions, a passive compliant section incorporating 'I'-shaped slits was specifically designed for the distal segment, allowing it to adapt to the curvature of the proximal segment. All the basic design parameters of the four tubes are listed in Table S1. The patterned slits were fabricated using high-precision laser cutting technology (HLR-PD0520-200IPG, Han's Laser, China). The diameter of laser beam is 30 micrometers and cutting power is 200 W, which means that the slits' width is also 30 micrometers. For welding (two tubes' tip), we used laser welding technology (SF150, Han's Laser, China).

Apart from the basic parameters of each tube (outer diameter R_o, inner diameter R_i and length of the steerable section L, shown in Figure S10 (A)), the geometric parameters of tenon-mortise slit parameters are optimized for simultaneous interlocking of inner/outer tube slits, thereby maximizing flexural rigidity and torsional stiffness during bending. As shown in Figure S10 (A), the tenon-mortise slits on one tube is determined by multiple parameters: central angle β representing the uncut area in cross section, length of tenon l_s, gap distance d_g between adjacent slits, number of slits N, number of tenon-mortise combination n in one slit, slit width d_s, height of slit d_h and tilted angle θ_s. Let $S_D = \{\beta, l_s, d_g, N, n, d_s, d_h, \theta_s\}$ denote the to-be-determined slit parameters for one single tube. S_D^o and S_D^i respectively represent the parameters for the outer tube and the inner tube. In the following, the subscript or superscript o and i respectively denote the parameter for the outer and the inner tube, and variables without subscript/superscript are applicable for both. The shape of the steerable section is assumed as an arch, and the dexterity for one segment can be mathematically expressed by the maximum bending curvature: $\kappa_m = \frac{\theta_m}{L}$, where θ_m is the maximum bending angle. When all the tenon-mortise slits interlock together, the bending angle reaches the maximum value θ_m, and we require the slits on the two tubes simultaneously reach the maximum value. As shown in Figure S10 (B), pushing/pulling the inner tube generates upward or downward bending. For the outer tube, the tenon-mortise slits extend while it bends upward, and the slits will compress when the segment bends downwards. Therefore, we can obtain the relationship between the parameters and the maximum bending angle:

$$\theta_m = \begin{cases} \theta_o^U = \frac{N_o d_s^o}{2 d_o \cos\theta_s^o} & \text{Upward} \\ \theta_o^D = \frac{N_o d_s^o}{2 d_o} & \text{Downward} \end{cases} \tag{1}$$

where θ_o^U and θ_o^D respectively denote the bending angles calculated from the outer tube in upward bending and downward bending modes. Similarly, for the inner tube, parts of design parameters are also related to the maximum bending angle:

$$\theta_m = \begin{cases} \theta_i^U = \frac{N_i d_s^i}{2 d_i} & \text{Upward} \\ \theta_i^D = \frac{N_i d_s^i}{2 d_i \cos\theta_s^i} & \text{Downward} \end{cases} \tag{2}$$

where θ_i^U and θ_i^U respectively denote the bending angles calculated from the inner tube in the two modes. As such, we can mathematically express the design goal that tenons and mortises on the two tubes simultaneously interlock together (the two tube reach the maximum bending angle concurrently): $\theta_o^U = \theta_i^D, \theta_o^D = \theta_i^U$.

With the diameters and steerable section's length of the tubes, we build the objective function to find the optimal design parameters:

$$\min .(\frac{1}{\kappa_m}) \tag{3}$$

This is to maximize the value of the maximum bending angle. The slit parameters are also mutually coupled. The number of slits and the slits' gap distance are related to the length of the steerable section: $N(d_s + d_g) = L$. For one slit, its length and the central angle β are related to the tube diameter: $(2l_s - \frac{2d_h}{\tan\theta_s})n = (2\pi - \beta)R_o$. Another constraint is built to require the two tubes to reach the maximum bending angle simultaneously ($\theta_o^U = \theta_i^D$): $N_o \frac{d_s^o}{\cos\theta_s^o} = N_i d_s^i$. Each design parameter should also fall within a given range: $S_{D\min} \leqslant S_D \leqslant S_{D\max}$. Table S2 lists the boundary values of each design parameter. Then, the optimization problem is solved using Genetic Algorithm with mixed integers in Matlab (Algorithm settings: population size 200, maximum iteration generation 4000, and elite number 60). The parameter central angle β directly relates to the stiffness, and we finalized its value through trial and error method (manufacture tubes with different β and other design parameters are kept same). The design parameters determining the 'I'-shaped slits are illustrated in Figure S10 (C), consisting of central angle β_I, gap distance d_g^I and height d_h^I. We set $d_g^I = d_g$ and $d_h^I = d_h$, and β_I is only variable to regulate the stiffness of the 'I'-shaped section. Through multiple trail-manufacturing, we finalize that $\beta_I = 2.87$ is the optimal value for stiffness. Finally, the design parameters of the tenon-mortise slits for the four tubes are finalized and listed in Table S3.

Finite Element Method (FEM) analysis was conducted in Ansys Workbench, and the two tubes were meshed using the default element size. The two tubes were bonded at the tip. The rigid section of the outer tube was exerted a fixed constrain, and a displacement of 2 mm was exerted to the inner tube to generate bending at the patterned section. The analysis is beneficial for initially validating the slits design method, and the results demonstrate that the slits of the two tubes interlock simultaneously. In a physical steerable arm, the slits of the inner tube (occluded by the outer tube) is invisible, so FEM is useful for design and initial evaluation.

Robot Kinematics

Kinematics model maps between the tip pose of robot arm and the base frame. The shape of the robot arm was assumed as an arch, and the geometric relationship between the bending angle and the push/pull distance was derived on the basis of work (*60*), which is therefore abbreviated. We then build the forward kinematics model through Homogeneous Transformation matrix. The shape of a single segment is assumed as an arch (Figure S12), and the shape parameters of the whole arm includes: $S = \{Q_p, \phi_p, \theta_p, Q_d, \phi_d, \theta_d\}$, where Q denotes translation DoF, ϕ is rotation angle and θ is bending angle (subscript p and d respectively denote the proximal segment and the distal). Therefore, the tip pose P in the robot base frame $\{B\}$ can be solved by homogeneous transformation:

$$\begin{aligned} {}^{P}_{B}T = T_z\left(Q_p\right) R_z(\phi_p) T_x(R_p) R_y(\theta_p) T_x(-R_p) \\ T_z\left(Q_d\right) R_z(\phi_d) T_x(R_d) R_y(\theta_d) T_x(-R_d) \end{aligned} \tag{4}$$

where $T_i\left(\cdot\right)$ and $R_i\left(\cdot\right)$ respectively denote translation homogeneous transformation and rotation homogeneous transformation matrix about axis i. Then P is mapped with shape parameters S: $P = f\left(S\right)$. In terms of the inverse kinematics, we aim to find the optimal shape parameters $\hat{S}$ to map with a given target tip point $\hat{P}$. We used constrained optimization approach to solve this hyper nonlinear problem, and can be initially set as:

$$\begin{aligned} \hat{S} &= \min \left\| f\left(S\right) - \tilde{P} \right\| \\ \text{w.r.t.} S_{\min} &\leq S \leq S_{\max} \end{aligned} \tag{5}$$

where $S_{\min} \leq S \leq S_{\max}$ constraints the boundaries of each DoF. To make the distal segment move with a larger distance in point-to-point movement, a penalty factor can be added at the loss function:

$$\hat{S}_k = \min \left[\left\| f\left(S\right) - \tilde{P}_k \right\| - \left(\theta^d_k - \theta^d_{k-1} - \theta^p_k + \theta^p_{k-1} \right) \right] \tag{6}$$

The constrained problem has six variables, and we employed Genetic Algorithm to obtain the optimal design parameters. In this optimization problem, we made following settings for Genetic Algorithm: population size is 50, the maximum iteration generation is 200, the elite count is 20, and the acceptable tolerance is 10^{-8}. To avoid jerky motion, robot system first computes the actuation configurations for the starting point and the end point, respectively, and then cubic interploration method is used to smoothen the variation of each motors. In addition, we used PID method to regulate the velocity.

3D-Printed Vertebral Phantom Model Preparation

We obtained the fluoroscopic data (DICOM format) for a patient from West China Hospital, Sichuan University, and reconstructed the 3D spinal geometry using 3D Slicer software. All patient-identifiable information was de-identified. Only the spinal structure was retained, which was then exported as a 3D model file (in STL format) for further processing. Finally, the model was fabricated using a 3D printer (X1, Bambu Lab, Shanghai, China) with polylactic acid (PLA) as the material.

In Vivo Animal Experiment Preparation

A 30-kg domestic pig (purchsed from Chengdu Dossy Experimental Animals CO., LTD.) was placed in the prone position (ventral recumbency) on an operation bed and secured with straps. Food was withheld for 12 h and water for 6 h prior to anesthesia to reduce gastric volume and the risk of regurgitation and aspiration. An intravenous catheter (20 G) was aseptically placed in the auricular vein for drug administration. All procedures were approved by the Animal Ethics Committee of West China Hospital, Sichuan University (Approval No. 2021794A), and were conducted in accordance with institutional guidelines for the ethical treatment and welfare of laboratory animals. General anesthesia was induced with an intramuscular combination of azaperone (2.0 mg/kg), midazolam (0.3 mg/kg), and butorphanol (0.3 mg/kg) to achieve sedation, anxiolysis and analgesia. After adequate sedation (10-15 minutes), vecuronium bromide (0.1 mg/kg IV) was administered to facilitate tracheal intubation. The pig was intubated with a 6.5–7.5 mm internal diameter endotracheal tube and ventilated mechanically. Anesthesia was maintained with desflurane at an inspired concentration of approximately 5% (1.0–1.3 MAC) in 100% oxygen using a closed-circuit vaporizer system. Ventilator settings included a tidal volume of 10 mL/kg and a respiratory rate of 12–15 breaths/min, adjusted to maintain end-tidal carbon dioxide ($EtCO_2$) between 35 to 45 mmHg. Additional vecuronium (0.015 mg/kg IV) was administered every 30~40 minutes to maintain neuromuscular blockade as required. Physiological monitoring included electrocardiography (ECG), non-invasive blood pressure (measured every 5 minutes), peripheral oxygen saturation (SpO_2), $EtCO_2$, end-tidal desflurane concentration and rectal temperature. Core body temperature was maintained between 37 to 39$^{\circ}C$ using a thermostatically controlled heating pad. Crystalloid fluid was infused intravenously at a rate of 7 mL/kg/h. If intraoperative signs of nociception (such

as tachycardia, hypertension) occurred, an additional dose of butorphanol (0.3 mg/kg) was administered. At the end of the experiment, surgical incisions were closed in layers. When the pig was still under deep anesthesia, it was euthanized humanely by intravenous injection of pentobarbital sodium (100mg/kg), in accordance with ethical guidelines to ensure minimal suffering.

Human Cadaver Tests Preparation

A single human cadaveric specimen was used in this study to validate the performance of the robotic system. The specimen was obtained from the Department of Anatomy, West China School of Medicine, Sichuan University, through a legally authorized body donation program. To strictly protect the donor's privacy and anonymity, specific demographic details (including exact age and medical history) are not disclosed. Pre-screening was performed to confirm the absence of gross pathologies or prior surgical interventions in the target lumbar region.

The specimen was preserved using a modified low-formalin embalming protocol derived from the Thiel method (*61*), which is optimized for maintaining tissue flexibility and biomechanical fidelity. Briefly, the vascular system was initially perfused via arterial infusion with a preservation solution containing <2% formaldehyde, polyols as cryoprotective agents, and balanced salts to maintain tissue hydration. Following initial stabilization, the specimen was stored at -20°C. Forty-eight hours prior to testing, the specimen was transferred to a temperature-controlled environment for gradual thawing at room temperature. Once fully thawed and rehydrated, the specimen was secured to a radiolucent carbon fiber operating bed to facilitate intraoperative imaging. The entire experimental protocol was approved by the Ethics Committee on Biomedical Research, West China Hospital of Sichuan University (Approval No. 2020554). All procedures were conducted in a controlled clinical simulation environment in accordance with institutional biosafety guidelines. The specimen was subjected to only a single freeze-thaw cycle to preserve the biomechanical fidelity of the soft tissues.

Statistical Analysis

For the path-following experiments, root mean square error (RMSE) and maximum error were calculated to evaluate tracking accuracy across repeated trials. Specifically, the optical sensing

collects the position of the markers ten times, and the mean value was utilized as the position data in the motion instance. All the quantitative data were plotted using Matlab (MathWorks, USA).

For stiffness characterization, force–displacement measurements were recorded and analyzed descriptively. In detail, the force data was obtained until the sensor readings were stable for at least 5 seconds.

For task performance, twenty repeated trials were conducted on the vertebral phantom model, with the success rate defined as the ability to reach key spinal targets within a single attempt.

Owing to the limited number of biological specimens (n=1 for both the human cadaveric specimen and the in vivo animal model), formal statistical hypothesis testing was not performed for these components of the study. Instead, the results are presented as feasibility assessments and qualitative validations. Procedural durations were extracted post-hoc via retrospective video analysis, and intraoperative blood loss was clinically estimated by the operating surgeon based on bleeding duration and anatomical site.

References and Notes

1. M. Gallucci, N. Limbucci, A. Paonessa, A. Splendiani, Degenerative disease of the spine. *Neuroimaging Clinics of North America* **17** (1), 87–103 (2007).

2. V. M. Ravindra, *et al.*, Degenerative lumbar spine disease: estimating global incidence and worldwide volume. *Global spine journal* **8** (8), 784–794 (2018).

3. M. Cheng, *et al.*, Global, Regional, and National Burden of Low Back Pain: Findings From the Global Burden of Disease Study 2021 and Projections to 2050. *Spine* **50** (7), E128–E139 (2025).

4. S. H. Farber, *et al.*, Complications associated with single-position prone lateral lumbar interbody fusion: a systematic review and pooled analysis. *Journal of Neurosurgery: Spine* **39** (3), 380–386 (2023).

5. T. A. Gionis, E. Groteke, Spinal decompression. *Orthopedic technology review* **5**, 36–39 (2003).

6. H. Yoshihara, Indirect decompression in spinal surgery. *Journal of Clinical Neuroscience* **44**, 63–68 (2017).

7. T. Karlsson, P. Försth, P. Öhagen, K. Michaëlsson, B. Sandén, Decompression alone or decompression with fusion for lumbar spinal stenosis: five-year clinical results from a randomized clinical trial. *The Bone & Joint Journal* **106** (7), 705–712 (2024).

8. F.-Y. Tsuang, Y.-L. Hsu, T.-Y. Chou, C. L. Chai, Long-term reoperation after decompression with versus without fusion among patients with degenerative lumbar spinal stenosis: a systematic review and meta-analysis. *The Spine Journal* (2024).

9. G. M. Overdevest, *et al.*, Effectiveness of posterior decompression techniques compared with conventional laminectomy for lumbar stenosis. *Cochrane database of systematic reviews* (3) (2015).

10. R. J. Mobbs, K. Phan, G. Malham, K. Seex, P. J. Rao, Lumbar interbody fusion: techniques, indications and comparison of interbody fusion options including PLIF, TLIF, MI-TLIF, OLIF/ATP, LLIF and ALIF. *Journal of spine surgery* **1** (1), 2 (2015).

11. Y.-H. Huang, C.-Y. Ou, Significant blood loss in lumbar fusion surgery for degenerative spine. *World neurosurgery* **84** (3), 780–785 (2015).

12. A. S. Hilibrand, M. Robbins, Adjacent segment degeneration and adjacent segment disease: the consequences of spinal fusion? *The Spine Journal* **4** (6), S190–S194 (2004).

13. Z. Pennington, *et al.*, Cost and quality of life outcome analysis of postoperative infections after posterior lumbar decompression and fusion. *Journal of Clinical Neuroscience* **68**, 105–110 (2019).

14. J. Allain, T. Dufour, Anterior lumbar fusion techniques: Alif, olif, dlif, llif, ixlif. *Orthopaedics & Traumatology: Surgery & Research* **106** (1), S149–S157 (2020).

15. K. Phan, M. Maharaj, Y. Assem, R. J. Mobbs, Review of early clinical results and complications associated with oblique lumbar interbody fusion (OLIF). *Journal of Clinical Neuroscience* **31**, 23–29 (2016).

16. H.-F. Zhu, *et al.*, Comparison of oblique lateral interbody fusion (OLIF) and minimally invasive transforaminal lumbar interbody fusion (MI-TLIF) for treatment of lumbar degeneration disease: a prospective cohort study. *Spine* **47** (6), E233–E242 (2022).

17. D. S. Xu, *et al.*, Minimally invasive anterior, lateral, and oblique lumbar interbody fusion: a literature review. *Annals of translational medicine* **6** (6), 104 (2018).

18. N. R. Khan, *et al.*, Surgical outcomes for minimally invasive vs open transforaminal lumbar interbody fusion: an updated systematic review and meta-analysis. *Neurosurgery* **77** (6), 847–874 (2015).

19. J. Zhang, *et al.*, Decompression using minimally invasive surgery for lumbar spinal stenosis associated with degenerative spondylolisthesis: a review. *Pain and Therapy* **10** (2), 941–959 (2021).

20. G. Choi, C. S. Pophale, B. Patel, P. Uniyal, Endoscopic spine surgery. *Journal of Korean Neurosurgical Society* **60** (5), 485–497 (2017).

21. A. Boaro, *et al.*, Efficacy and safety of flexible versus rigid endoscopic third ventriculostomy in pediatric and adult populations: a systematic review and meta-analysis. *Neurosurgical review* **45** (1), 199–216 (2022).

22. B. Carl, M. Bopp, B. Saß, C. Nimsky, Microscope-based augmented reality in degenerative spine surgery: initial experience. *World neurosurgery* **128**, e541–e551 (2019).

23. A. G. Bishop, T. L. Uhl, J. B. Zwischenberger, S. L. Meyerson, Prevalence and impact of musculoskeletal pain due to operating among surgical trainees. *Journal of Surgical Education* **80** (5), 676–681 (2023).

24. B. Z. Chin, *et al.*, Full-endoscopic versus microscopic spinal decompression for lumbar spinal stenosis: a systematic review & meta-analysis. *The Spine Journal* **24** (6), 1022–1033 (2024).

25. C.-C. Ko, P.-H. Lee, J.-S. Lee, K.-Z. Lee, Spinal decompression surgery may alleviate vasopressor-induced spinal hemorrhage and extravasation during acute cervical spinal cord injury in rats. *The Spine Journal* **24** (3), 519–533 (2024).

26. R. Härtl, *et al.*, Worldwide survey on the use of navigation in spine surgery. *World neurosurgery* **79** (1), 162–172 (2013).

27. A. Picciariello, A. Annicchiarico, G. Gallo, A. Dezi, U. Grossi, Evaluation of the da Vinci single-port system in colorectal cancer surgery: a scoping review. *Updates in Surgery* **76** (7), 2515–2520 (2024).

28. F. Celotto, *et al.*, Da Vinci single-port robotic system current application and future perspective in general surgery: A scoping review. *Surgical Endoscopy* **38** (9), 4814–4830 (2024).

29. K. Bach, *et al.*, Morphometric analysis of lumbar intervertebral disc height: an imaging study. *World neurosurgery* **124**, e106–e118 (2019).

30. M. H. Lee, *et al.*, Comparative Outcomes of Biportal Endoscopic Decompression, Conventional Subtotal Laminectomy, and Minimally Invasive Transforaminal Lumbar Interbody Fusion for Lumbar Central Stenosis. *Neurospine* **21** (4), 1178 (2024).

31. K. J. Nicholson, B. A. Winkelstein, Nerve and nerve root biomechanics. *Neural Tissue Biomechanics* pp. 203–229 (2010).

32. R. Li, *et al.*, Functional Outcomes After 'SHURUI' Single-Port Robot-Assisted Pyeloplasty for Uretero Pelvic Junction Obstruction: Single-Centre Experience. *The International Journal of Medical Robotics and Computer Assisted Surgery* **21** (2), e70056 (2025).

33. F. Wang, *et al.*, FIORA: A flexible tendon-driven continuum manipulator for laparoscopic surgery. *IEEE robotics and automation letters* **7** (2), 1166–1173 (2021).

34. T. Kato, I. Okumura, S.-E. Song, A. J. Golby, N. Hata, Tendon-driven continuum robot for endoscopic surgery: Preclinical development and validation of a tension propagation model. *IEEE/ASME Transactions On Mechatronics* **20** (5), 2252–2263 (2014).

35. J. Davy, *et al.*, Magnetic Fluid-Driven Vine Robots for Minimally Invasive Tissue Biopsy Sampling. *Advanced Intelligent Systems* p. 2400827 (2025).

36. M. Ghevondyan, M. Davtyan, M. Aghayan, Dielectric elastomer actuators: Medical applications review. *Discover Materials* **5** (1), 43 (2025).

37. X. Wang, *et al.*, A Magnetic Catheter With Force Sensing Capability Toward Interventional Surgery. *IEEE Robotics and Automation Letters* (2024).

38. K. Price, *et al.*, Using robotics to move a neurosurgeon's hands to the tip of their endoscope. *Science robotics* **8** (82), eadg6042 (2023).

39. M. F. Rox, *et al.*, Mechatronic design of a two-arm concentric tube robot system for rigid neuroendoscopy. *IEEE/ASME transactions on mechatronics* **25** (3), 1432–1443 (2020).

40. T. E. Ertop, *et al.*, Towards Suturing From Within the Urethra Using Concentric Tube Robots: First Experiences in Biological Tissues, in *2022 International Symposium on Medical Robotics (ISMR)* (IEEE) (2022), pp. 1–5.

41. J. Tian, T. Wang, X. Fang, Z. Shi, Design, fabrication and modeling analysis of a spiral support structure with superelastic Ni-Ti shape memory alloy for continuum robot. *Smart Materials and Structures* **29** (4), 045007 (2020).

42. M. Tummers, *et al.*, Continuum concentric push–pull robots: A Cosserat rod model. *The International Journal of Robotics Research* p. 02783649241263366 (2024).

43. J. A. Childs, C. Rucker, A Kinetostatic Model for Concentric Push–Pull Robots. *IEEE transactions on robotics* **40**, 554–572 (2023).

44. T. L. Bruns, *et al.*, A modular, multi-arm concentric tube robot system with application to transnasal surgery for orbital tumors. *The International Journal of Robotics Research* **40** (2-3), 521–533 (2021).

45. A. R. Lanfranco, A. E. Castellanos, J. P. Desai, W. C. Meyers, Robotic surgery: a current perspective. *Annals of surgery* **239** (1), 14–21 (2004).

46. M. J. Mack, Minimally invasive and robotic surgery. *Jama* **285** (5), 568–572 (2001).

47. M. Diana, J. Marescaux, Robotic surgery. *Journal of British Surgery* **102** (2), e15–e28 (2015).

48. G. Fang, *et al.*, Clinical application of Renaissance spine robot assisted system in spinal disease. *Chinese Journal of Orthopaedic Trauma* pp. 299–303 (2017).

49. M. Bhimreddy, *et al.*, Accuracy of Pedicle Screw Placement Using the ExcelsiusGPS Robotic Navigation Platform: An Analysis of 728 Screws. *International Journal of Spine Surgery* **18** (6), 712–720 (2024).

50. E. Summerside, J. Heller, J. Glenn, B. McCormack, P. P. M. Menchetti, Tissue sparing posterior fixation as a treatment option for degenerative disc disease, in *Cervical Spine: Minimally Invasive and Open Surgery* (Springer), pp. 231–245 (2022).

51. I. Busscher, J. J. Ploegmakers, G. J. Verkerke, A. G. Veldhuizen, Comparative anatomical dimensions of the complete human and porcine spine. *European spine journal* **19** (7), 1104–1114 (2010).

52. Q. He, *et al.*, Clinical Results of Oblique Lateral Interbody Fusion OLIF Technique Compared with Conventional Lumbar Posterior Laminar Decompression for Lumbar Spinal Stenosis. *Biomedical Journal of Scientific & Technical Research* **43** (3), 34497–34503 (2022).

53. Q. Huang, *et al.*, A retrospective cohort study comparing perioperative clinical outcomes and radiographic results between patients undergoing TLIF and OLIF surgeries. *BMC surgery* **25** (1), 188 (2025).

54. J. Wang, *et al.*, Design of a multi-arm concentric-tube robot system for transnasal surgery. *Medical & biological engineering & computing* **58** (3), 497–508 (2020).

55. T. Vandebroek, *et al.*, Macro-micro multi-arm robot for single-port access surgery, in *2019 IEEE/RSJ international conference on intelligent robots and systems (IROS)* (IEEE) (2019), pp. 425–432.

56. R. J. Webster III, B. A. Jones, Design and kinematic modeling of constant curvature continuum robots: A review. *The International Journal of Robotics Research* **29** (13), 1661–1683 (2010).

57. Y. Li, D. H. Myszka, A. Murray, The kinematics of constant curvature continuum robots through three segments. *IEEE Robotics and Automation Letters* **8** (11), 7631–7638 (2023).

58. L. Hou, *et al.*, A Sensing Strategy Combining Kinematic Model with FBG Sensors for Continuum Robots. *IEEE Transactions on Instrumentation and Measurement* (2025).

59. B. Ahmad, P. A. Floor, I. Farup, C. F. Andersen, Single-image-based 3D reconstruction of endoscopic images. *Journal of Imaging* **10** (4), 82 (2024).

60. K. Oliver-Butler, J. A. Childs, A. Daniel, D. C. Rucker, Concentric push–pull robots: Planar modeling and design. *IEEE Transactions on Robotics* **38** (2), 1186–1200 (2021).

61. W. Thiel, Supplement to the conservation of an entire cadaver according to W. Thiel. *Annals of anatomy= Anatomischer Anzeiger: official organ of the Anatomische Gesellschaft* **184** (3), 267–269 (2002).

Acknowledgments

Funding: This work was funded by the 1·3·5 project for disciplines of excellence, West China Hospital, Sichuan University (ZYYC21004), the Postdoctor Research Fund of West China Hospi-

tal, Sichuan University (2025HXBH057) and the Sichuan Provincial Natural Science Fundation (2026NSFSC1240).

Author contributions: Qingxiang Zhao conceived the robotic system idea, designed the instruments and organized this paper. Xiandi Wang proposed the clinical demand and led all the medical-related experiments. Runfeng Zhu and Xin Zhong respectively designed the mechanical structure and the electronic part of the system. Dan Pu supported all the medical-related environments. Baitao Lin, Tao Li, Shiyuan Sui, Haonan Zhou and Yuxi Cheng worked in clinical trials and preparation for the experiments. Henry K. Chu organized the structure of this manuscript, designed the robot-related experiments and polished the text. Hao Zheng and Peizhi Zhou worked in experiments and writing. Jiancheng Zeng supervised and instructed all the trials. Kang Li supported the whole project and polished this manuscript.

Competing interests: Authors declare no competing interest.

Data, code and materials availability: All data needed to evaluate the conclusions in the paper are present in the main text or the Supplementary Materials. The data and code for this study have been deposited in the database Dryad (doi:10.5061/dryad.08kprr5gm).

No new materials were developed in this study.

Supplementary Materials for

A Minimally-Invasive Robotic Spinal Surgical System for Anterior Lumbar Nerve Decompression

Qingxiang Zhao[†], Xiandi Wang[†], Xin Zhong, Runfeng Zhu, Peizhi Zhou, Dan Pu, Baitao Lin, Tao Li, Shiyuan Sui, Haonan Zhou, Yuxi Cheng, Hao Zheng, Henry K. Chu, Jiancheng Zeng[*], Kang Li[*]

[*]Corresponding author. Email: likang@wchscu.cn, and tomzeng5@163.com

[†]These authors contributed equally to this work.

This PDF file includes:

Supplementary Results

Figures S1 to S12

Tables S1 and S4

Captions for Movies S1 to S5

Other Supplementary Materials for this manuscript:

Movies S1 to S5

Supplementary Results

Table S1. Basic Tube Design Parameters (Unit: mm).

	Proximal Segment		Distal Segment	
	Outer Tube	Inner Tube	Outer Tube	Inner Tube
OD	2	1.7	1.4	1.1
ID	1.8	1.5	1.2	0.9
Tenon-mortise Section Length	15	15	18	18
Passive Compliant Section Length (Figure S9-③)	0	0	48	48
Rigid Section Length (Figure S9-①)	124	118	80	76
Passive Compliant Section Length (Figure S9-⑤)	73	84	107	114
Rigid Section Length (Figure S9-②)	256	312	376	434

Table S2. Boundary values of tenon-mortise slits design parameters. 'Constant' means the parameter is predefined.

Variable	Minimum	Maximum	Variable	Minimum	Maximum
L (mm)	Constant		N (integer)	1	1000
Tubes OD (mm)	Constant		n (integer)	1	1000
Tubes ID (mm)	Constant		d_s	0.03	0.06
β (°)	15	50	d_h	0.25	0.3
l_s (mm)	0.1	0.7	θ_s	45	75
d_g (mm)	0.3	0.6			

Table S3. Design parameters of slits for the four tubes.

	Proximal Segment		Distal Segment	
Design Parameter	Outer Tube	Inner Tube	Outer Tube	Inner Tube
β (rad)	0.35	0.36	0.35	0.35
l_s (mm)	0.59	0.56	0.44	0.49
d_g (mm)	0.51	0.31	0.50	0.50
N	27	41	34	32
n	4	4	6	3
d_s (mm)	0.036	0.054	0.03	0.06
d_h (mm)	0.26	0.26	0.28	0.31
θ_s (rad)	1.02	1.03	0.87	1.05

Table S4. Tip Deviation for the single proximal segment and the dual-segment arm under various actuation settings and loads (Unit: mm).

Push Distance Applied	Only Proximal Segment		Dual Segment	
on the Inner Tube	20g Load	50g Load	20g Load	50g Load
1 mm	2.46	3.51	8.92	12.6
2 mm	2.31	2.42	9.56	13.5
3 mm	1.64	2.12	11.3	16.8

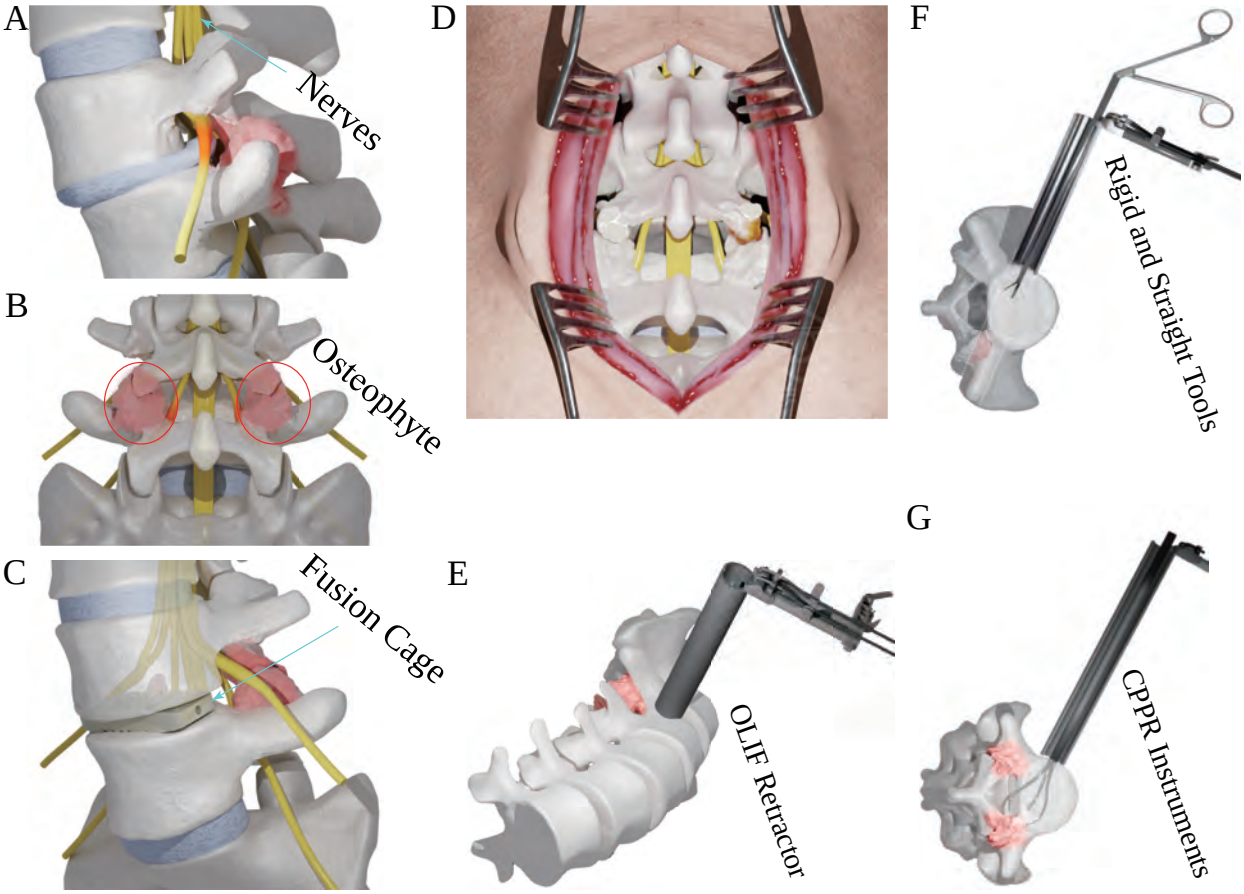

Figure S1. **Basics of lumbar degenerative diseases, existing surgical approach and our robot-assisted treatment method.** (A) Degenerative spinal structures compress lumbar nerves, so patients feel pain in the lower back and legs. (B) Rear view of spine. Osteophyte at the articular joint processes compressed nerves. (C) Implant a fusion cage in intervertebral disc to expand space for the nerves and restore stability of spine. (D) Posterior method to resect the degenerative structures, which needs an incision port of around 8 cm in length, and intraoperative blood loss is around 300 to 500 mL. (E) OLIF approach. Build a corridor using OLIF retractor to enable instruments to reach the front side of vertebrate. (F) Rigid and straight surgical tools enter the space of intervertebral disc but the surgeon has limited operation space and occluded visual field, leading to incomplete and indirect decompression outcome. (G) Use CPPR-based dexterous instruments to pass through the intervertebral disc and completely resect the degenerative structures at the posterior and anterior areas of spine.

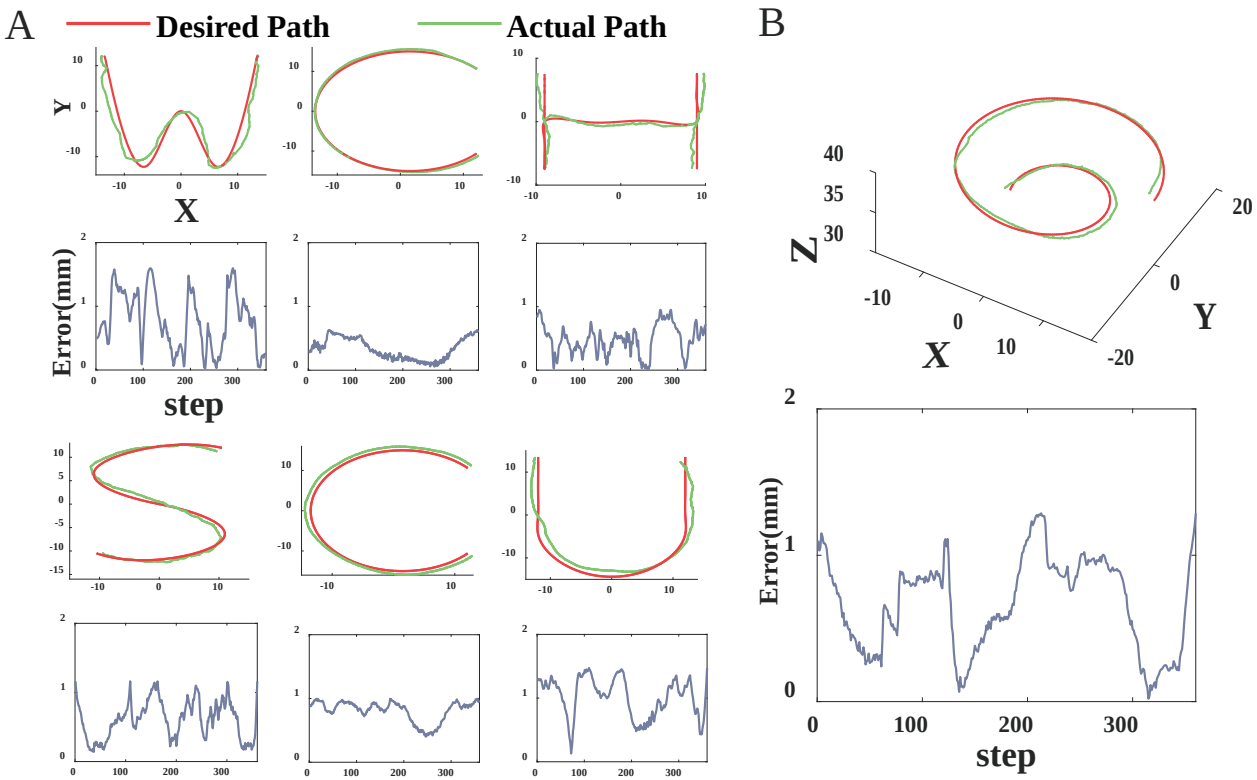

Figure S2. **Path-following task and tip position error. The velocity of the tip marker is around 9 mm/s. Lower velocity will contribute to higher accuracy.** (A) 2D path following results and error. (B) 3D path following result and error.

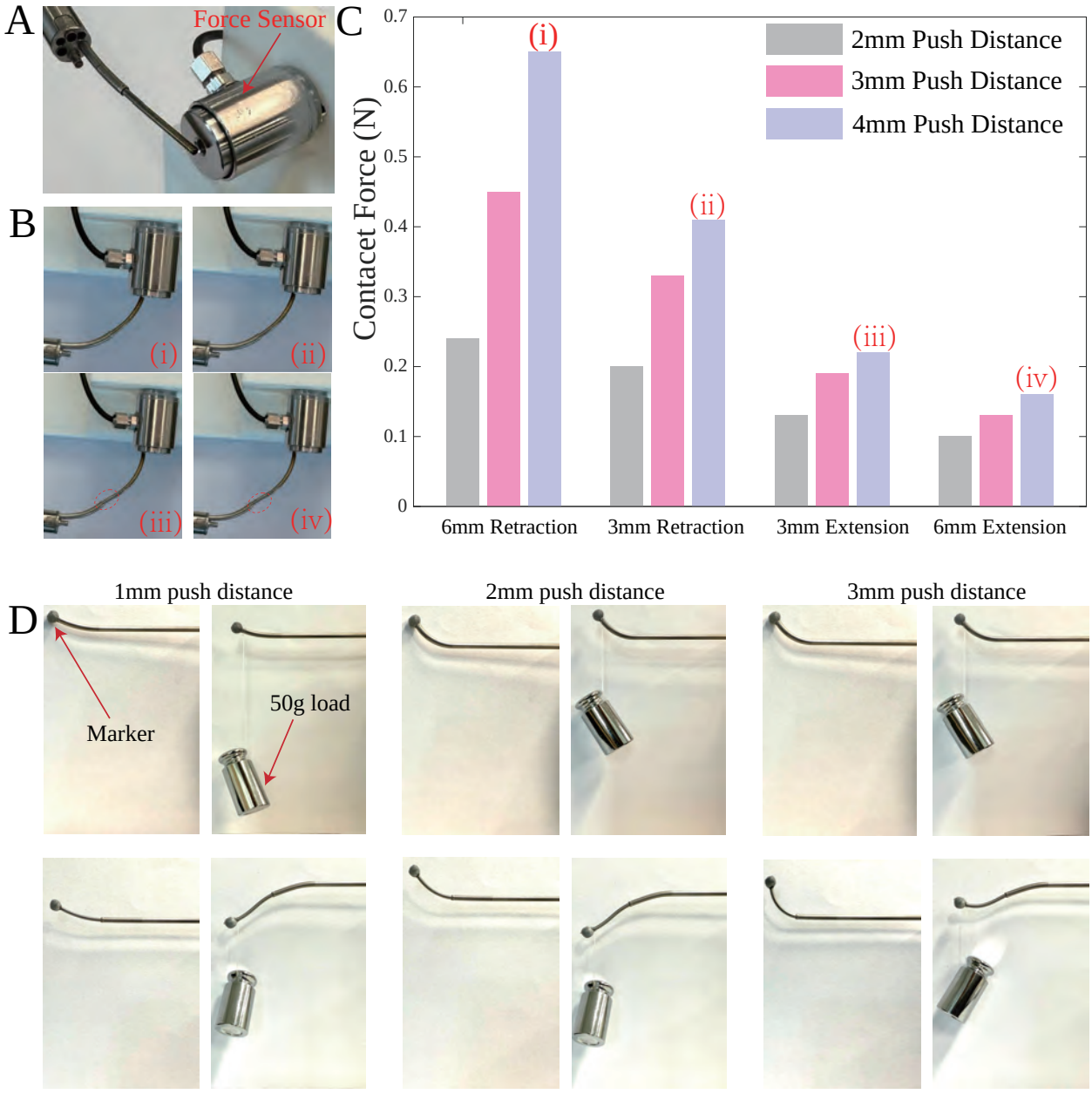

Figure S3. **Stiffness tests on the whole arm.** (A) Experiment setup for testing the stiffness of the dual-segment robot arm. (B) Key snapshots of one dual-segment robot arm interacting with the force sensor. While the passive compliant section of the distal segment extends from the proximal segment, larger push distance acting on the inner tube generates more notable deformation (highlighted in red dashed ellipse). In load-free scenario, the passive compliant section is straight, but it also deforms to adapt with obstacles, which is friendly to manipulate delicate tissues, such as nerves. (C) Snapshots of the robot arm in load-free and with-load scenarios. The position deviation between the two scenarios shows the ability of withstanding payload.

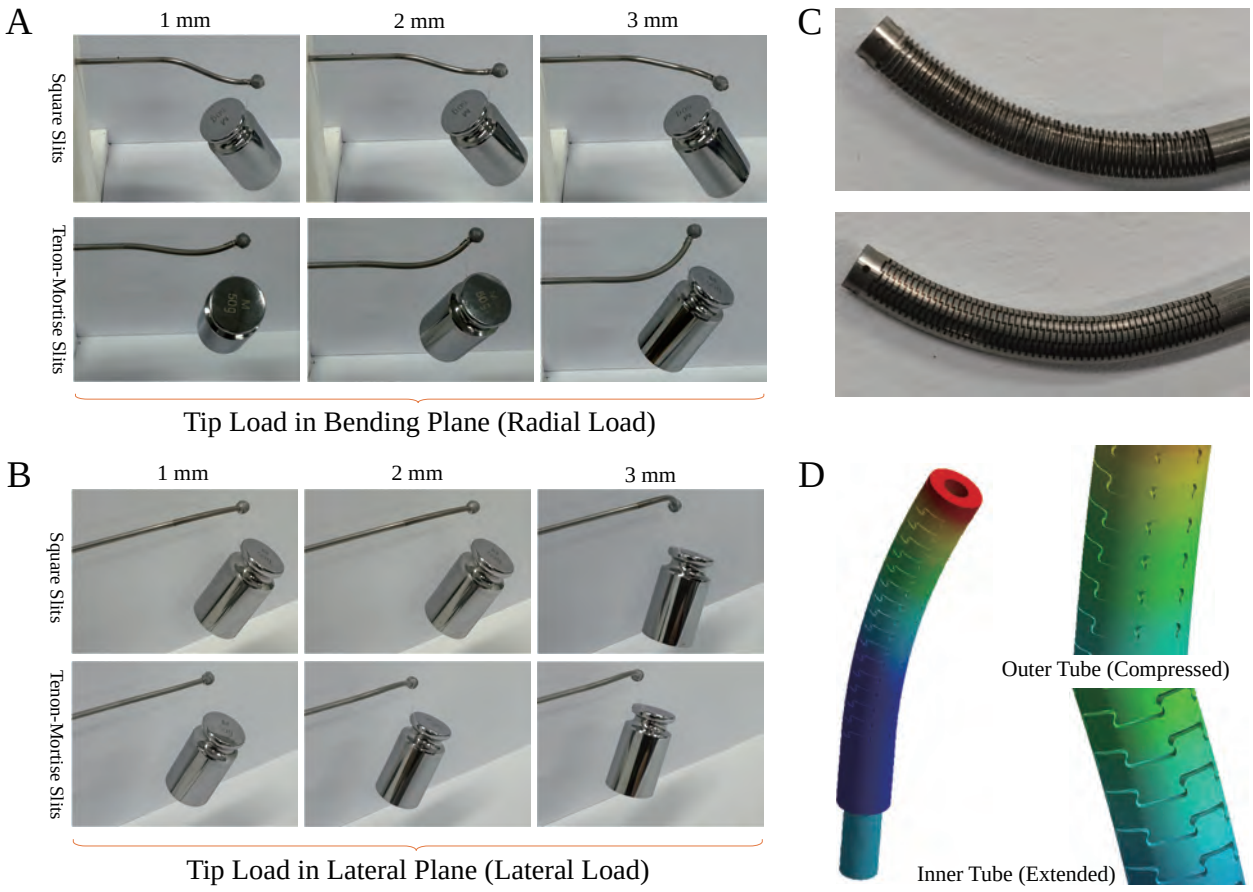

Figure S4. **Stiffness comparison between tenon-mortise and square-slit CPPR arms (identical dimensions except slit type).** (A) One load of 50 g was hung at the tip to generate radial load. (B) One load of 50 g was hung to generate lateral load. (C) Comparison of square slits and tenon-mortise slit in bending shape, and the tenons and mortises interlock together. While for the square slits design, much of the area is vacated. (D) FEM analysis results about the tenon-mortise slits design, and the slits on both the inner tube and the outer tube simultaneously interlock together.

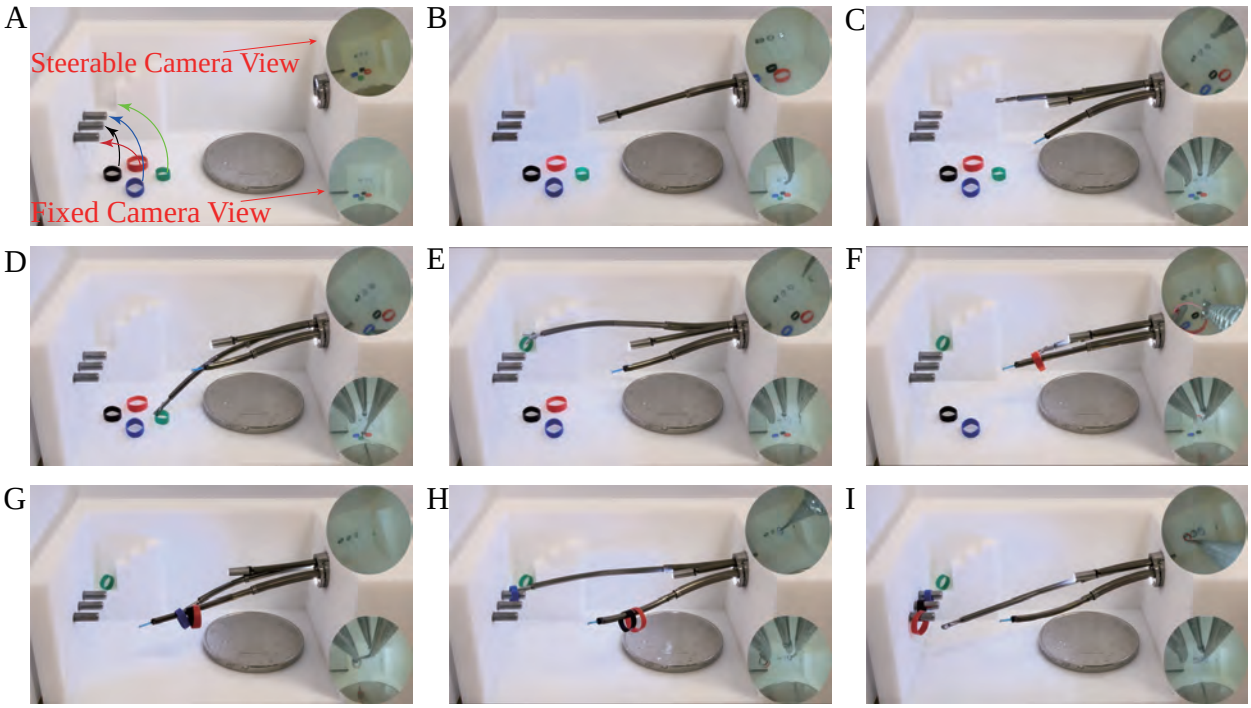

Figure S5. **Key snapshots illustrating multi-arm coordination.** (A) The three robotic arms are commanded to collect and place four rubber rings to specific targets sequentially under endoscopic view as guidance. A coin is placed to show the narrow task space to provide a scale reference. (B) Extension of the steerable camera arm. (C) The three steerable instruments all extend from the trocar and reach the task space. (D) The gripper arm is picking up the green rubber ring. (E) Placement of the green rubber ring into a $3 \times 3 \times 3$ mm semi-closed corner. (F) Retrieval of the red rubber ring and its hanging on the laser optical fiber arm. (G) Completion of ring collection and hanging on the laser arm. (H) Sequential retrieval of the rubber rings for placement onto three target columns. (I) Successful placement of all rubber rings at their designated targets.

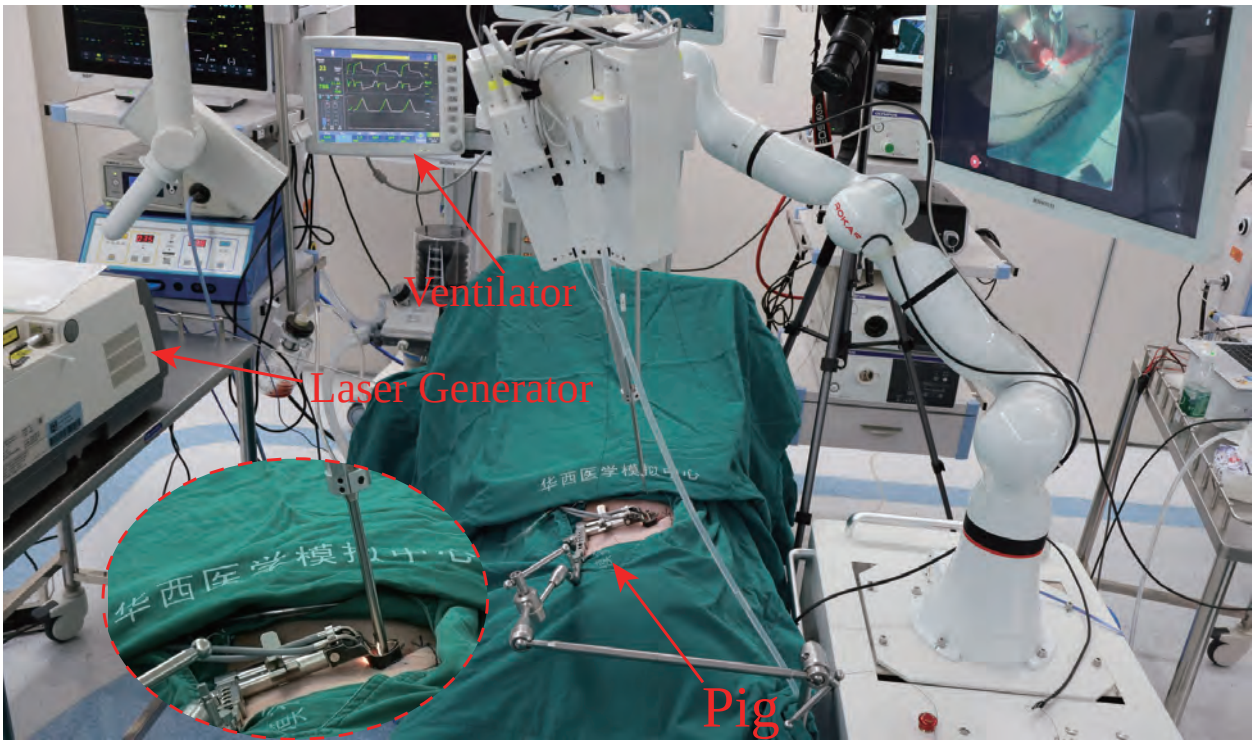

Figure S6. **In vivo animal experiment setup.** A standard OLIF retractor was employed to build the corridor. Ventilator always monitored the key parameters of the pig. The robot system was arranged beside the operating bed, and the pig was in right body position. Thulium laser generator provided energy for hemostasis and for resection.

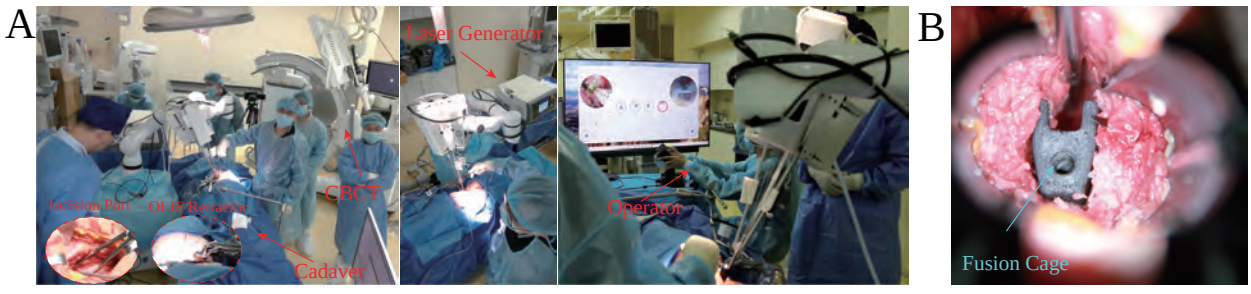

Figure S7. **Human cadaver tests setup.** (A) Operation room setting. The CBCT collected fluoroscopic images to confirm the surgical targets. (B) Implant a fusion cage at the vacated intervertebral disc space after decompression procedure.

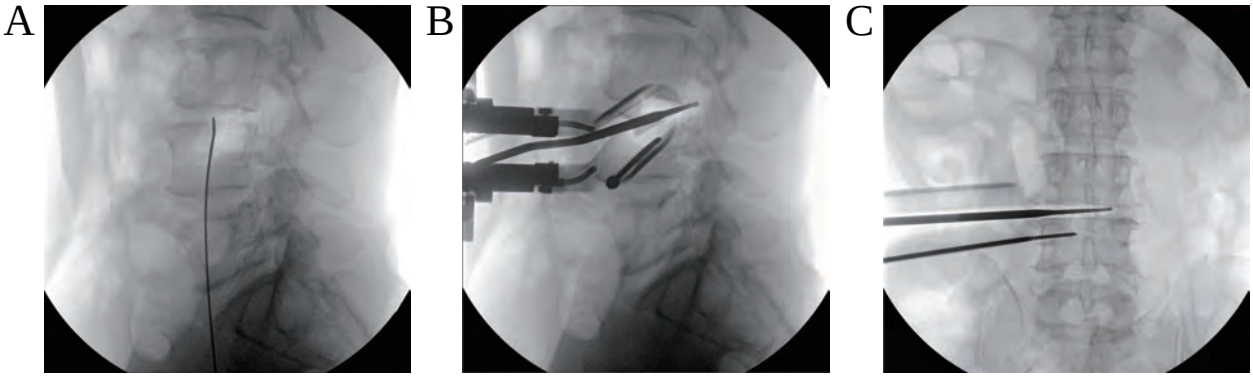

Figure S8. **Fluoroscopic images for confirming the surgical site.** (A) Lateral view of spine after inserting a guidewire at the target intervertebral disc. (B) Lateral view of spine after building the corridor by the retractor. (C) Posterior view of spine with a straight dissector inserted.

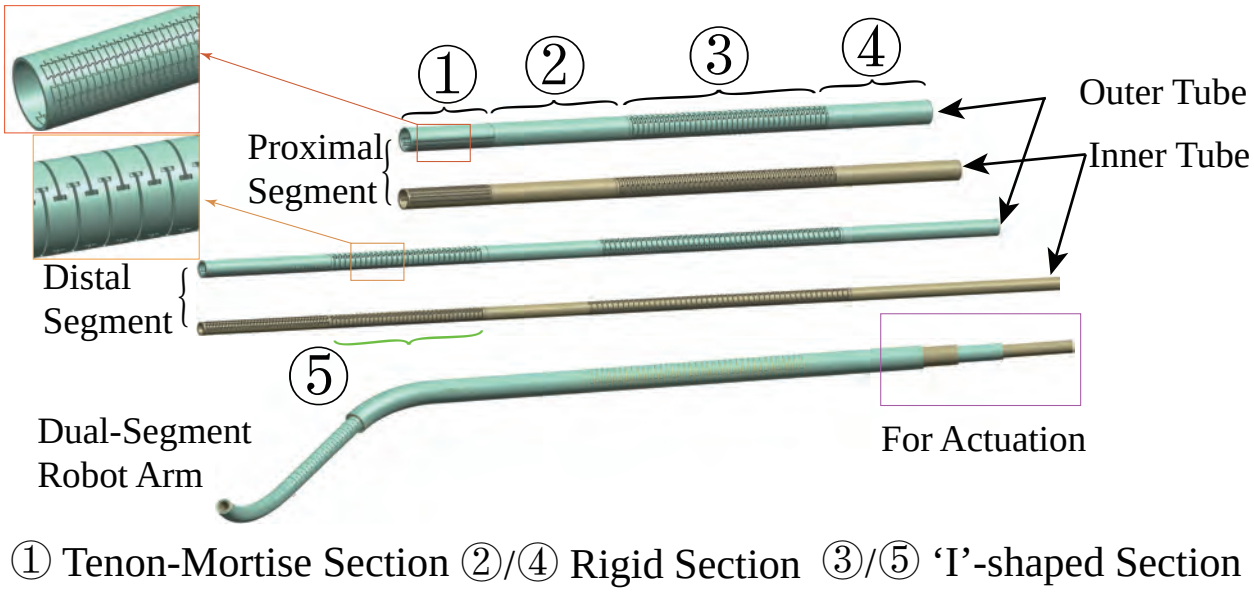

Figure S9. **Basic illustration of four hollow steel tubes forming one dual-segment robot arm.** Each segment consists of a pair of tubes that are fixed at the tip. For the proximal segment, each tube has 4 sections from the tip to the end, including tenon-mortise section, rigid section, 'I'-shaped section and actuation section. For the distal segment, it has an additional 'I'-shaped section to passively adapt with the shape of the proximal segment. At the end, the rigid section was designed for actuation (labeled by pink box).

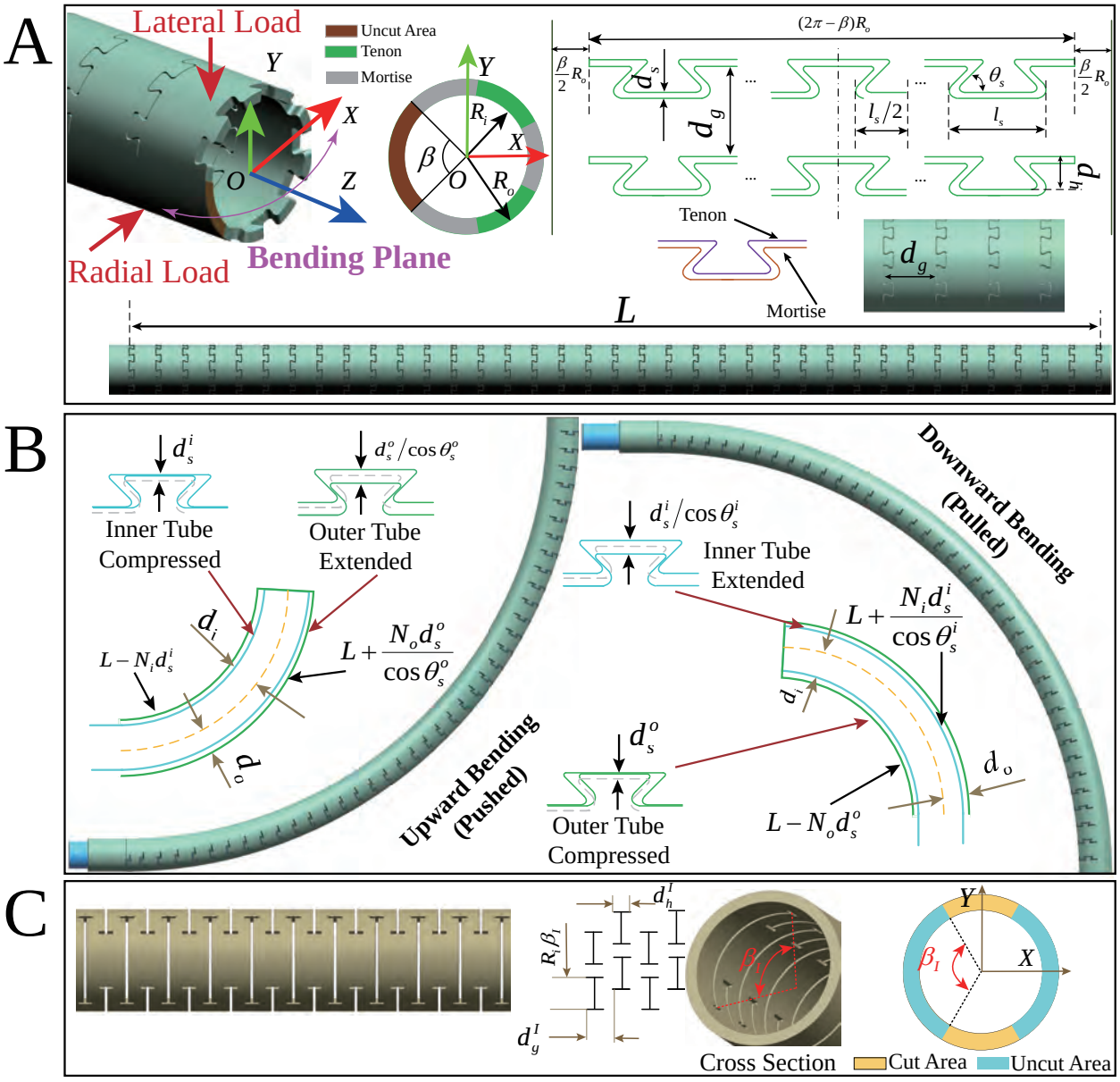

Figure S10. **Detailed design parameters of one segment.** (A) Parameters of tenon-mortise slits. (B) For one bendable segment, pushing or pulling the inner tube generates 2D arc bending at the patterned section. The tenon-mortise slits on the two tubes are both required to interlock together simultaneously, enhancing rigidity. (C) Parameters of the 'I'-shaped section.

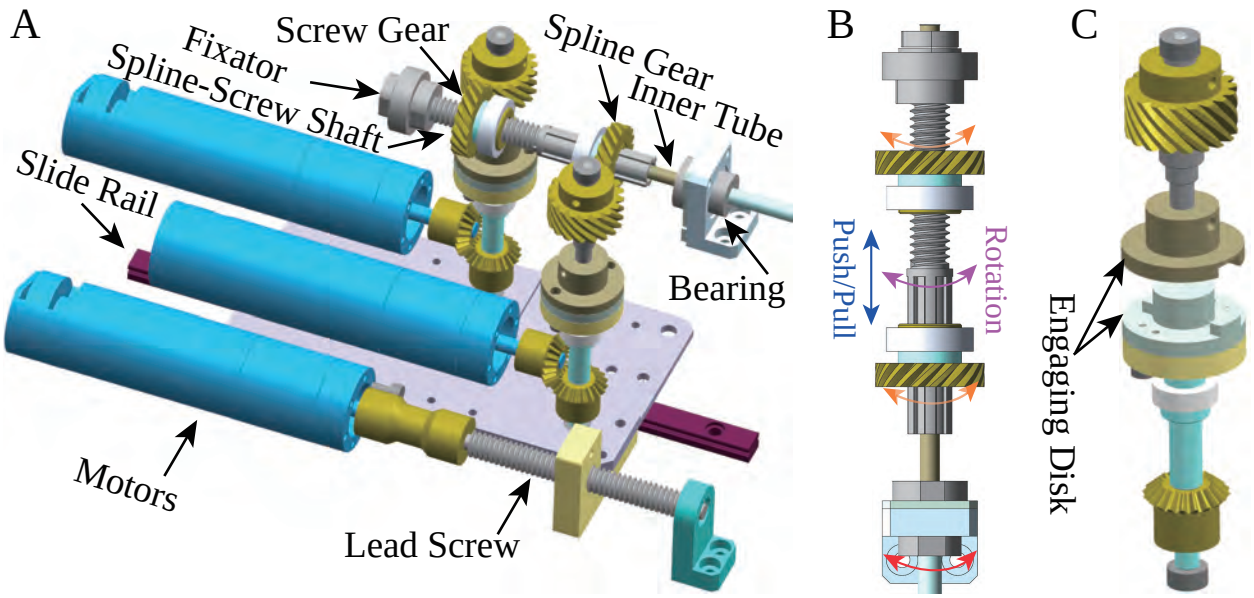

Figure S11. **key actuation module for a single segment.** (A) The outer tube is fixed on a bearing, and the inner tube is fixed on a spline-screw shaft. One DC motor rotates a lead screw to realize translation of the whole module. (B) Two gears (a spline gear and a screw gear) are respectively assembled on the shaft. Once the two gears rotate at an equal velocity (labeled by orange arrows), the shaft rotates accordingly (purple arrow). When the screw gear rotates and the spline gear keeps static, translational motion is achieved and the inner tube is being pushed or pulled (blue arrow). Two pairs of helical gear transmit motion from the motors. (C) For quick release/assembly, we designed engaging disk structures on the instrument component and the actuation component. The angle gear connects with a DC motor.

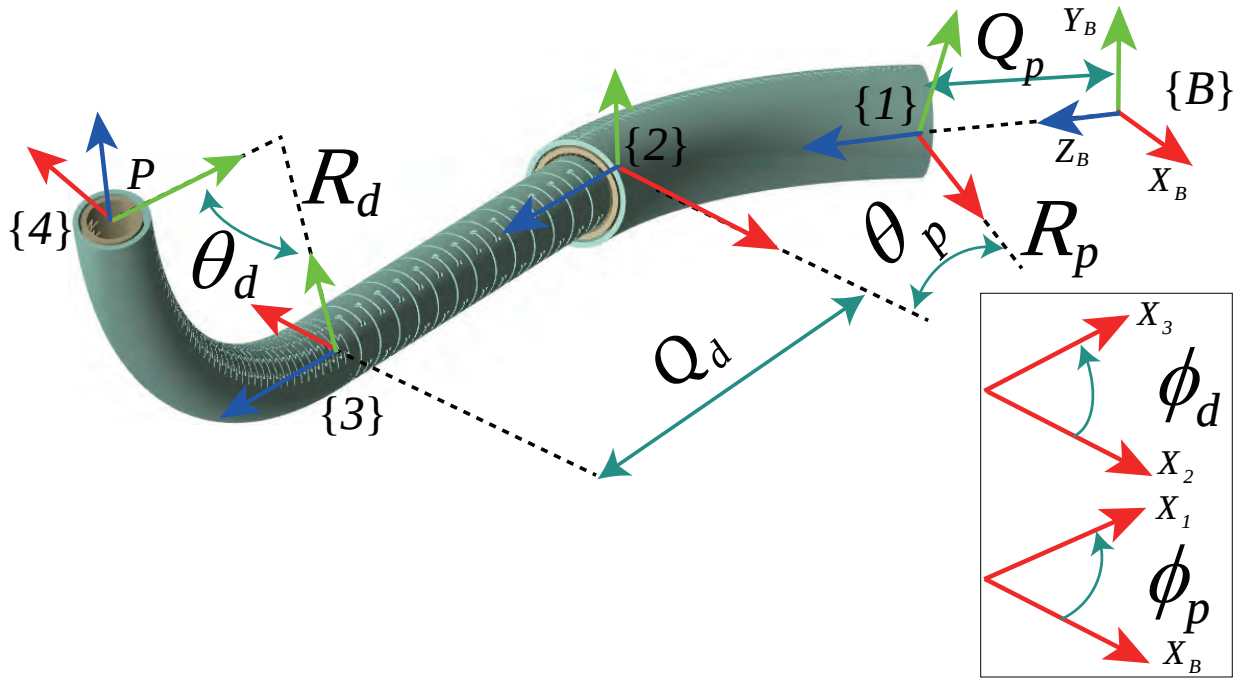

Figure S12. **Kinematics modeling of the dual-segment robot shape.** For a robot arm, the shape of each segment is assumed as an arch, so the robot tip position with respective to the base frame can be accordingly solved via the shape parameters. Translation, rotation and bending DoFs are expressed by Q, ϕ and θ, respectively.

Table S1. Detailed Tube Design Parameters (Unit: mm).

Table S2. Boundary values of tenon-mortise slits design parameters. 'Constant' means the parameter is predefined.

Table S3. Design parameters of slits for the four tubes.

Table S4. Tip Deviation for the single proximal segment and the dual-segment arm under various actuation settings and loads (Unit: mm).

Movie S1. Basics of the robot system. This video shows the process of assembling one instrument component on the actuation component, which only needs around 20s for quick exchange instruments in surgery. In addition, the motion of each instrument is shown, including motion of any single robot arm and their coordination.

Movie S2. Performance of a single robot arm. A dual-segment robot arm follows various paths, and the capability of carry weight is shown in this video.

Movie S3. Arm-Arm coordination and animation about key decompression procedures. Dexterous slender instruments collect small rubber rings and place them sequentially to targets, and the endoscopic camera views are the only visual feedback for the operator. During surgery, the gripper functions to dissect and grip tissues, and the laser optical fiber arm cauterizes veins to stop bleeding and resect degenerative spinal structures.

Movie S4. In vivo animal experiment. Robotic instruments incise the intervertebral disc of a porcine spine and reached the posterior area.

Movie S5. Human cadaver tests. Videos from the endoscopic cameras to show the key procedures of decompression in a cadaver.